Arktos (2015) 1:10
DOI 10.1007/s41063-015-0009-5

ORIGINAL ARTICLE

A new age model for the Central Arctic reveals brief intervals of extreme sedimentation rates over the last 140 kyr

Wesley B. Myers[1] · **Dennis A. Darby**[1]

Received: 15 September 2015 / Accepted: 23 October 2015 / Published online: 20 November 2015

Abstract A detailed age model for central Arctic sediments (Mendeleev Ridge) reveals remarkably high sedimentation rates of >20 cm kyr^{-1} during brief intervals during the last 140 kyr. This age model is developed using a modified event stratigraphy based on changes in source provenance, mineral, and geochemical variations that are correlated from a core with a detailed age model on the Yermak Plateau near Fram Strait (HLY0503-22JPC) to a core on the Mendeleev Ridge (HLY0503-9JPC). The Yermak core has a previously determined age model linked to the global δ^{18}O ice volume record. The age model presented here indicates that the average sedimentation rate in core 9JPC is only ~2 cm kyr^{-1}, but brief periods of intense sediment accumulation range up to >20 cm kyr^{-1}. Many of these events are identified to be basin-wide and possibly associated with major freshwater or ice-rafting events indicating that these events are tied to climatic glacial/interglacial processes. During marine isotope Stage 3 for instance, an ice-rafted detritus event contemporaneous with Heinrich event 4 is identified and can be linked to a large-scale event by precise source determinations using the chemical fingerprint of detrital, ice-rafted Fe oxide grains. The provenance indicates that this event is contemporaneously sourced to three major regions of Arctic glaciation. There are other rapid sedimentation events that are not correlated to both cores and these must be from localized melt-out events from either icebergs or sea ice.

Keywords Arctic · Sediment age · Sedimentation rates · Mineralogy · Sediment chemistry · Fe oxide provenance

Introduction

The Arctic region plays an important role in the regulation of the global climate [1, 28]. Thus, it is imperative to understand the timing of events in this polar region in order to identify if and how Arctic changes are linked to global climate changes. Accurate age control is needed to establish synchronous basin-wide events or the history of climate change across the Arctic. Modeling experiments also require improved age dating of climate events than is currently available, especially in the central Arctic. Thus, accurate understanding of the timing of events in this region is crucial to understanding the past and predicting future climate change.

The difficulty in applying traditional chronostratigraphic methods along with the need for accurate chronostratigraphy in this highly important region emphasizes the need for alternative methods to provide age control here where traditional methods of chronostratigraphy have failed. For most of the world's oceans, chronostratigraphy is, or can be fairly well established using, for example: stable isotopes, radiocarbon, biostratigraphy, paleomagnetic stratigraphy, and lithostratigraphy [9, 11, 34, 39, 59, 62, 63]. One of the most commonly used methods is that of stable oxygen isotopes (δ^{18}O). With these data, marine isotope stages (MIS) were defined to produce a high-resolution Pliocene–Pleistocene-type section with which all paleoceanographic sediment records can be compared ([42]; LR04). A direct correlation of most Arctic continuous isotope stratigraphic records to the LR04 benthic age model stack is precluded by the unique environmental conditions of the Arctic

---

✉ Wesley B. Myers
wmyer002@odu.edu

[1] Old Dominion University, 4600 Elkhorn Avenue, Norfolk, VA 23508, USA

region [3]. The large Arctic freshwater influence via extraordinary volumes of riverine input, glacial ice disintegration as well as brine rejection from sea ice formation often results in the overprinting of $\delta^{18}O$ isotopic signatures [39, 58]. Additionally, there is a problem with the sporadic occurrence of benthic foraminifera in Arctic sediments, due to limited biological activity, low biodiversity, and high rates of calcareous test dissolution in the deep waters of the central Arctic Ocean [3, 4].

Another commonly used proxy for age, paleomagnetism, is also problematic in the Arctic due to difficulty in defining paleomagnetic secular variation in this region [64]. The proper identification of reversals or excursions has been an issue in past studies. For example, Clark et al. [9] utilized a paleomagnetic reversal, identified as the Brunhes/Matuyama boundary, and lithology to produce a lithostratigraphy that could be applied over large distances. This reversal was later challenged and determined to not be a full reversal but rather a paleomagnetic excursion, either the Biwa II [29] or the 'Pringle Falls event' [62]. Alternatively, the paleomagnetic variation in Arctic sediments might be related to diagenetic changes [69, 70]. The unique bottom water chemistry of the Arctic Ocean can diagenetically alter the fine-grained magnetic fraction of the sediment record and thus the paleomagnetic record. Regardless of the paleomagnetic issue, several studies have shown that lithostratigraphy and other physical and geochemical properties can be used to correlate cores over great distances [2, 57, 59, 62]. Traditional dating methods used to constrain ages in sediment cores such as radiocarbon for the last 40 kyr, biostratigraphy, and to an extent paleomagnetic variation are insufficient for the central Arctic region due to the perennial sea ice cover, low productivity, large freshwater input, and unique bottom water chemistry [3].

Chronostratigraphy is essential for all paleoceanographic studies because understanding the timing of events is a critical first step in the interpretation of the sediment record. Because of the slow and highly variable rates of deposition in the central Arctic [2, 4, 30, 33, 49, 51, 56], placing Arctic sediments in a regional or global time frame requires closely spaced age dates that just are not available in the central Arctic [53]. Development of chronostratigraphy for sediment records in the Arctic has been a persistent problem ever since the first Arctic cores were recovered from the early ice camps [9]. This issue has been especially true for the central and western portions of the Arctic basin, where a long-standing debate persisted as to whether this region was sediment starved or not. It is now generally thought that the central Arctic region is likely not 'sediment starved,' but chronostratigraphy for this region is still problematic and poorly constrained [3, 4]. High-resolution records are uncommon, and high-resolution records that extend past the Last Glacial Maximum (LGM) are even more rare.

Previous studies found regional differences in the geology of the coastal areas surrounding the Arctic Ocean [22, 66, 68], suggesting that mineralogical and geochemical variations in central Arctic sediment records can be used to determine transport pathways. For example, Fe oxide detrital grain chemistry can be precisely sourced to 41 circum-Arctic sources and be used to determine the position of the Transpolar Drift (TPD) and the Beaufort Gyre (BG) through time [6, 12, 17, 21, 23, 24, 62]. Here we build on these previous findings and use this information on drift pathways to develop correlations between cores along the drift path. Quaternary age models for the western and central Arctic Ocean (Amerasian Basin) are mostly restricted to poorly constrained biostratigraphy [11], lithostratigraphy [9, 62], physical properties [57], Mn stratigraphy [43–45], cyclostratigraphy [5], and other low precision dating techniques [4, 51]. Therefore, this study develops an age model for the central Arctic Ocean sediments using an approach based on the precise sources of detrital, anhydrous Fe oxide minerals (Fe grains) and distinct down-core mineral and geochemical variations. More specifically, this work attempts to transfer an age model from a well-dated core from the Fram Strait area (Yermak Plateau) that extends to ca. 140 ka to a Mendeleev Ridge core, separated by a distance of ~2200 km. These two cores were chosen because they are ideally located to record major variations in the dominant ice drift pathways. The basic premise is that ice-rafted detritus (IRD) from unique sources will deposit similar sediment markers in both the Mendeleev Ridge area and the Yermak Plateau as a result of climate-controlled variations in the surface circulation of the Arctic Ocean.

Methods

Sediment cores

The cores examined in this study were collected during the second leg of the Healy-Oden Trans-Arctic Expedition 2005 (Table 1) [19]. The cores were photographed and analyzed onboard the ship for gamma-density, p-wave velocity, and magnetic susceptibility via a GeoTek Multi-Sensor Core Logger. Grain size was analyzed by a Malvern Mastersizer 2000 on ~0.25 g samples, corresponding to Fe grain samples. Core HLY0503-9JPC (Mendeleev Ridge; 79°35.605′N, 172°27.663′W; 2783 m water depth; henceforth 9JPC) was selected as the western Arctic core to which the age model is correlated (Fig. 1). This core site is uniquely situated at the confluence of the Transpolar Drift (TPD) and the Beaufort Gyre (BG). The TPD is a

Table 1 Core information for 22JPC and 9JPC

	HLY0503-22JPC	HLY0503-9JPC
Location	Yermak Plateau	Mendeleev Ridge
Latitude	80°29.386′N	79°35.605′N
Longitude	7°46.141′E	172°27.663′W
Water depth (m)	798	2783
Core length (m)	13.31	15.4
	Sampling Interval Ranges (min–max) (cm)	
Physical properties	1	1
Textural analysis	1–10	2–16
Fe grain matches	1–10	1–12
Quantitative mineralogy (XRD)	1–10	2–8
Geochemistry (XRF)	0.5–4	0.9–6

Location, analyses, and sampling resolution ranges for each analysis

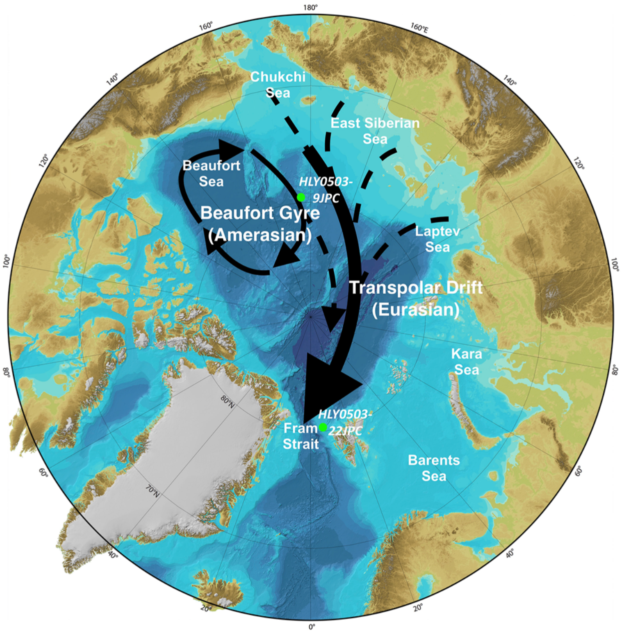

Fig. 1 Map of the Arctic Ocean region highlighting the present-day circulation regime that consists of the Transpolar Drift and the Beaufort Gyre. Core locations are plotted (*green dots*). Map is modified from Jakobsson et al. [28]

prominent surface current that carries primarily Eurasian sediment entrained by ice across the Arctic to Fram Strait. The BG is an anticyclonic circulation gyre and during interglacial periods is restricted to the Canada Basin and is dominated by sediments entrained primarily from North America, but with occasional influx of IRD from Russia [23]. 9JPC has been correlated to several very similar cores along the Alpha–Mendeleev Ridge system using lithology, geochemical signatures, and physical sediment parameters [20, 51]. Thus an updated age model for JPC09 might be transferable to other central Arctic cores.

Core HLY0503-22JPC (80° 29.386′N, 007°46.141′E; 798 m water depth; henceforth 22JPC) was retrieved from the Yermak Plateau in Fram Strait (Fig. 1). This core location is in the pathway of sea ice exiting the Arctic Ocean, meeting warmer North Atlantic waters that facilitate melting and sediment deposition (Fig. 1). The unique location of this core, in the Fram Strait, permitted the construction of a detailed age model by correlation of a paleomagnetic intensity proxy to the LR04 $\delta^{18}O$ record [70].

Core sampling

Sediment density is a direct reflection of the mineralogy, grain size, and compaction of the sediments, and thus we used large variations in the mean density to guide sampling for mineralogical analysis because they might help identify distinct mineral variations. Each core was sampled at slightly different resolution depending on the method of analysis. Accounting for all parameters measured, the sampling resolution range for 22JPC was 1–10 cm, with higher-resolution sampling in sections with the largest variability. Similarly in 9JPC, the sampling range was 0.9–16 cm with the sections with the largest density of variation sampled in more detail (Table 1).

Fe grain matching

The Fe grain chemistry (14 elements) for ~100 Fe grains/sample is used to determine the precise source of each Fe grain [13, 24]. All samples were wet-sieved at 45, 63, and 250 µm. The magnetic portion of the 45–250 µm fraction is used for analysis of detrital anhydrous Fe oxide grains [24]. In short, each magnetic grain is analyzed on an electron probe micro-analyzer to determine the composition of Fe, Ti, O, Mn, Mg, Ca, Si, Al, Ni, Cr, V, Zn, Ta, and Nb, and then matched to the source data set. The accuracy of this method is determined from rigorous tests to be <2 % error of mismatch [24].

Quantitative bulk mineralogy

Bulk mineralogy of the <45 µm fraction was determined through X-ray diffraction (XRD) of randomly oriented powder mounts. Using <45 µm fraction is favored as it provides information regarding the bulk mineralogy, as opposed to just the clay fraction (<2 µm). By examining the <45 μm fraction the overwhelming quartz signal from the coarsest material is avoided while still retaining the bulk mineralogical signal. Randomly oriented XRD mounts are preferred to oriented ones, because the latter may bias the mineralogical composition, especially the non-clay minerals [48]. Details of the methods and procedures used in this study can be found in Srondon et al. [60] and Eberl [26].

A brief synthesis of these methods is as follows: 1 g of a well-mixed <45 μm sample is mixed with 0.25 g of powdered, 99.9 % pure corundum which serves as an internal standard. This mixture is ground in a McCrone Micronizing mill for 5 min with 4 ml of methanol and subsequently oven-dried overnight at 80 °C. The dried sample is sieved through a 400- to 500-μm sieve for homogenization. The sample is milled for ten minutes with three 10-mm acrylic balls in a ball mill to further enhance sample homogeneity. Next ~0.3 mL of hexane (0.5 mL per gram of pure clay) is added and the sample is mixed again for 10 min in the ball mill. The sample is dried under a fume-hood, passed through the sieve again, and side mounted in special powder mounts for XRD using frosted glass to help ensure random orientation. The samples analyzed on a Panalytical X'Pert PRO XRD with a Cu-tube from 5° to 65° 2θ with 0.2° steps at 2 s per step (45 mA, 40 kV). The sample pattern is transferred to the program RockJock, which integrates mineral intensity factors of known standards in the program's library to calculate and match the pattern of the unknown sample, thus converting the samples mineral constituents into weight percent [25]. This program is shown to be accurate and precise, where values are ±4 % of the actual values [25]. Independent tests of the RockJock program on random mineral mixtures all fell to ±4 % or better of the actual values.

X-ray fluorescence

XRF is used to monitor the variability of major and minor elements in numerous central Arctic cores [10]. In brief, an Innov-X Alpha Series 4000 XRF hand held instrument was used to analyze each of the cores. It uses a 40 kV, tungsten X-ray source coupled with a SiPiN diode detector and a 170 mm^2 aperture window. Prior to and after each core analysis, the instrument was calibrated using NIST standards. Each core was analyzed for 25–30 elements, of which 13 were consistently above instrument detection limits. Of these 13 elements, only 7 were used in this study as these were either deemed to be least reactive and thus less affected by diagenesis (K, Ti, Co, Rb, and As) or the most useful for correlating between cores as they relate to major lithologic changes (Ca and Mn). The former geochemical group was used for the correlation, while the latter was reserved for environmental interpretation of 9JPC.

22JPC age model

The age model for 22JPC was based on the changes in the grain size of magnetite that mimics the global oxygen isotope curve [70]. These authors identified a grain-size proxy for this mineral in the form of κ_{ARM}/κ, anhysteretic remanence susceptibility over total magnetic susceptibility. The κ_{ARM}/κ ratio closely resembles the stacked global benthic $\delta^{18}O$ record ([42]; LR04). This similarity is presumed to be due to sea-level fluctuations during glacial periods where eustatic sea levels drop, which in turn restricted the size and volume of the Arctic Ocean basin and constricts the current flow at Fram Strait [70]. Thus, during a glacial interval there will be coarser magnetite in the Fram Strait sediments as increased current velocities winnow the finer-grained materials. During an interglacial, however, with higher sea levels, the Fram Strait current velocity decreases allowing finer-grained material to accumulate, thus changing the magnetic susceptibility [70].

The grain-size proxy record for MIS stratigraphy allows for the direct correlation of LR04 age model stack to 22JPC (Fig. 2a) [70]. Where fauna were available for $\delta^{18}O$ analysis, these results confirmed the paleomagnetic proxy [70]. In addition, two Holocene samples at 100.5 cm and 138 cm were ^{14}C dated to 15.34 and 18.50 ka, respectively. Using a reservoir correction of 440 years and the calibration of Nowaczyk et al. [50], these ages are 17.71 and 21.35 ka, respectively (Fig. 2b). There is an offset between the $\delta^{18}O$ and the κ_{ARM}/κ ratio at the MIS 2/1 boundary of >10 cm that is likely from $\delta^{18}O$ depletion resulting from the early deglaciation of the Svalbard region [37]. This might impart some uncertainty at other glacial to interglacial transitions given the proximity of the core site to the Svalbard/Barents Ice Sheet, but overall the record compares remarkably well with the LR04 $\delta^{18}O$ record. The correlation picks were then fit to the 22JPC record via a piecewise cubic hermite interpolating polynomial fit (PCHIP, Fig. 2c), which preserves the shape of the curve and does not make estimations outside the bounds of the data. The κ_{ARM}/κ record was plotted against the 22JPC age model and yielded improved correspondence to the LR04 $\delta^{18}O$ record (Fig. 2c). The resulting 22JPC age model was then used in conjunction with the Fe grain provenance data, mineralogical data, and geochemical data to transfer ages to the 9JPC sediment record. The overall potential error for the 22JPC age model would be tied to the error of the LR04 benthic stack; this error is estimated to be no more than 4 kyr (non-accumulating) for the last 1 Ma [42]. Obviously, the error is less for the last 140 kyr.

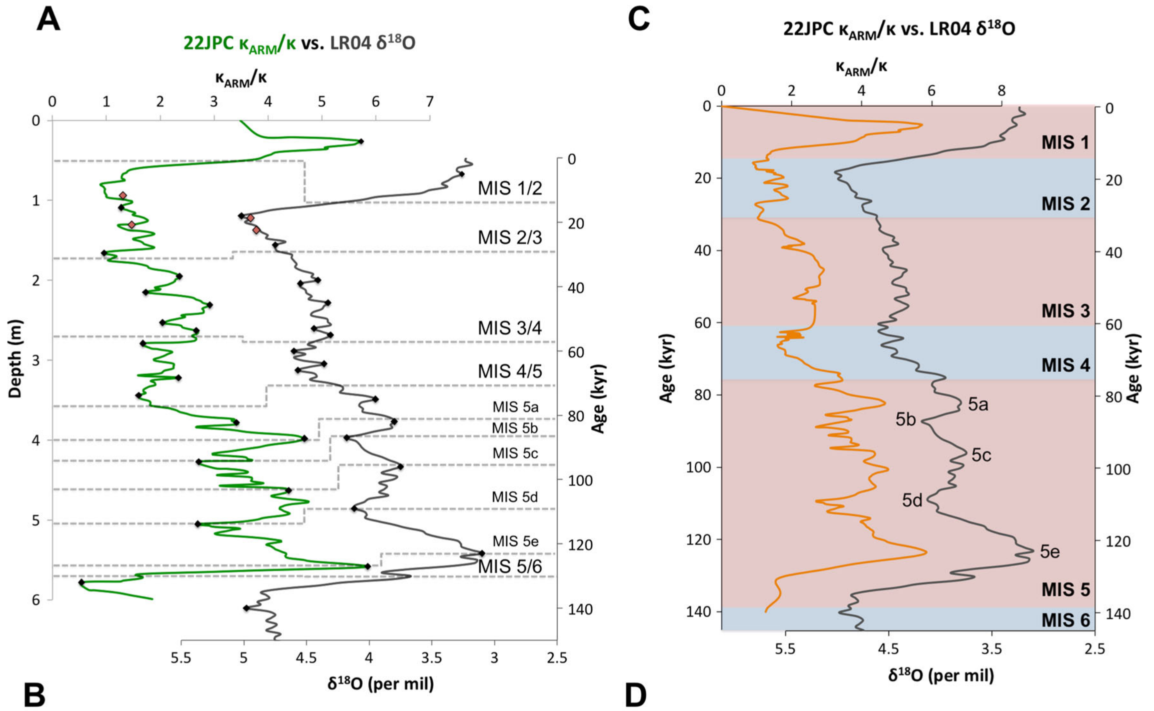

B

List of Correlated Points			
22JPC Depth (cm)	LR04 Age (kyr)	22JPC Depth (cm)	LR04 Age (kyr)
26	5	279	62
100.5	17.71*	322	64
109	18	344	66
138	21.35*	378	75
166	27	398	82
195	38	427	87
215	39	463	96
231	45	505	109
253	53	558	123
273	55	578	140

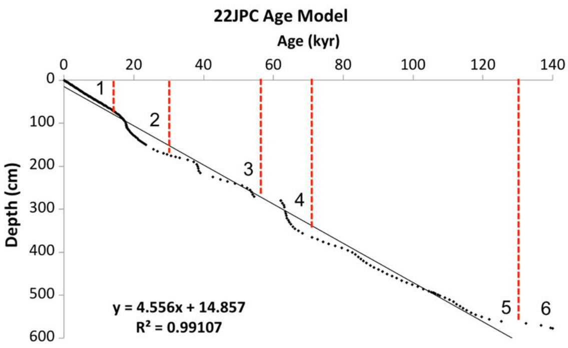

Fig. 2 22JPC age model, modified from Xuan et al. [70] using the LR04 record as the index [42]. **a** Comparison plots of the κ_{ARM}/κ magnetic grain-size proxy (*green*) and the LR04 δ^{18}O benthic stack, with MIS indicated [42]. **b** Table of correlation points, * denotes AMS-^{14}C dated material [70]. **c** Realignment of the κ_{ARM}/κ magnetic grain-size proxy and LR04 δ^{18}O benthic stack. MIS labeled and glacial (*blue*) and interglacial (*red*) conditions indicated. **d** 22JPC age model

Results and discussion

9JPC age model

In order to produce an age model for 9JPC, a lithologic index variable was needed to correlate the two cores. The index identified is that of the ratio of Fe grains rafted by the TPD to those rafted by the BG. 9JPC is located at the confluence of the TPD and BG and 22JPC in the eastern Fram Strait is in the path of exiting ice drift. The temporally stable structure of these surface currents averaged over hundreds to thousands of years combined with changes in the ratio of the two Fe grain signals based on the provenance data for these Fe grains can be used to monitor the glacial/interglacial climate variability. During an interglacial, the 9JPC core site will receive material from TPD sources (Eurasia) as well as North American material from the BG where the two drift currents join (Fig. 1) [14]. This signal of Eurasian and North American material is transported to Fram Strait and deposited at core site 22JPC. During glacial periods, a change in surface circulation has been proposed where the BG shifts toward North America and instead of mingling with the TPD, flows directly to the western Fram Strait (Fig. 3) [6, 61]. The result of this circulation reconfiguration would be the loss of the TPD–BG mixing, and both 9JPC and 22JPC will receive Eurasian material almost exclusively. Iceberg scours have been identified in the Chukchi Plateau region, which indicates

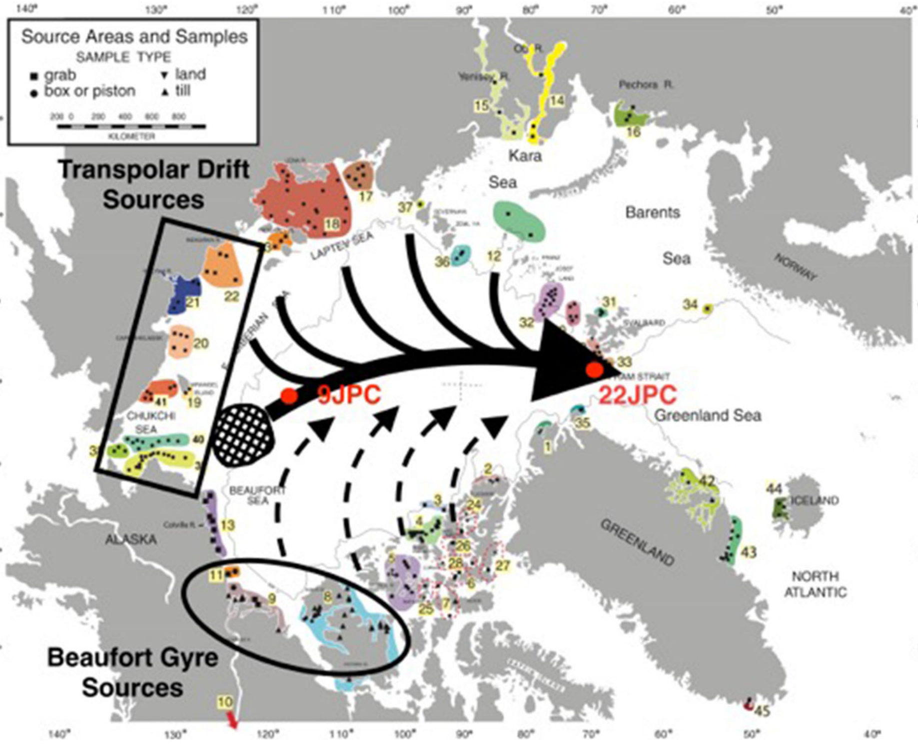

Fig. 3 Arctic map showing the possible glacial period surface circulation patterns [61]. Core locations are highlighted in *red*. The source groups used for the TPD/BG ratio are *highlighted*. TPD comprised of Chukchi and East Siberian Seas, and representing the easternmost sources in the TPD and potential source of a Chukchi-based ice sheet [33]. BG sources comprised of the Canadian Arctic Archipelago and northern Alaska, and representing the Laurentian and Innuitian Ice Sheets. The *crosshatched section* indicates location of potentially grounded ice, determined via identification of glacial and iceberg-turbated diamicton and glaciogenic features [31, 33, 52]

that large ice blockages might have existed here during the LGM (Fig. 3) [33]. This ice would have further prevented BG sourced material from being delivered to 9JPC. Thus, the result of these climatically driven differences will be a lower TPD/BG ratio during interglacial intervals as there is more exchange between the BG and TPD and a higher ratio during glacial periods, as the TPD will dominate both core locations except for rare iceberg purges from the Laurentide Ice Sheet [15, 18]. Such changes are clearly seen in both cores and provide the guidelines for the 22JPC-9JPC correlations (Fig. 4).

To produce this TPD/BG index, the weighted percent of Fe grain matches [24] attributed to TPD and BG specific sources were grouped and a ratio was calculated. The TPD sources are identified in Fig. 3 and constitute Fe grains matched to the East Siberian and Chukchi Seas. The other common sources of TPD sediment, the Laptev, and Kara Seas were not included, as to isolate only those sources that have drift paths consistently crossing the Mendeleev Ridge. The BG material primarily consists of the Canadian Arctic Archipelago, Mackenzie River, and the northern coast of Alaska, all of which are strong sources of sediment in the Beaufort Sea during both interglacial and glacial periods [15, 21, 22]. Comprised of shelf, coastal, riverine, and river delta sediments, a total of 8 and 4 specific source areas were combined for the TPD and BG, respectively (Fig. 3).

In general, the TPD/BG ratios range from 0.05 to 6.15 for 22JPC and 0 to 0.85 for 9JPC (Fig. 4). Due to the closer proximity of 9JPC to BG sources and the potential for mixing of the two currents, the TPD/BG ratio values in 9JPC are generally lower than what is seen in the 22JPC record. The exception being during glacial periods when the BG Fe grains reaching 9JPC will be low and TPD Fe grains dominate.

Mineralogy and geochemistry

The TPD/BG ratio was examined to distinguish major climatic changes and identify potential matches between the cores. In general, for each peak/trough identified in the 9JPC TPD/BG index, two to three corresponding peaks were identified in 22JPC. These peaks/troughs were then examined for similar mineralogical and geochemical content variation in order to refine the initial correlations. For the intervals between the TPD/BG correlated points, the mineralogical and geochemical data identify additional correlations.

A total of 29 source samples were analyzed for quantitative mineralogy to distinguish mineral variability along the margins of the Arctic Ocean. Three specific mineral species, dolomite, plagioclase, and smectite, were identified to have unique provenance attributed to the Canadian Arctic Archipelago, East Siberian and Laptev Seas, and the Laptev and Kara Seas, respectively (Fig. 5). Thus, these mineral species were determined to be the most useful in identifying corresponding peaks in both 22JPC and 9JPC.

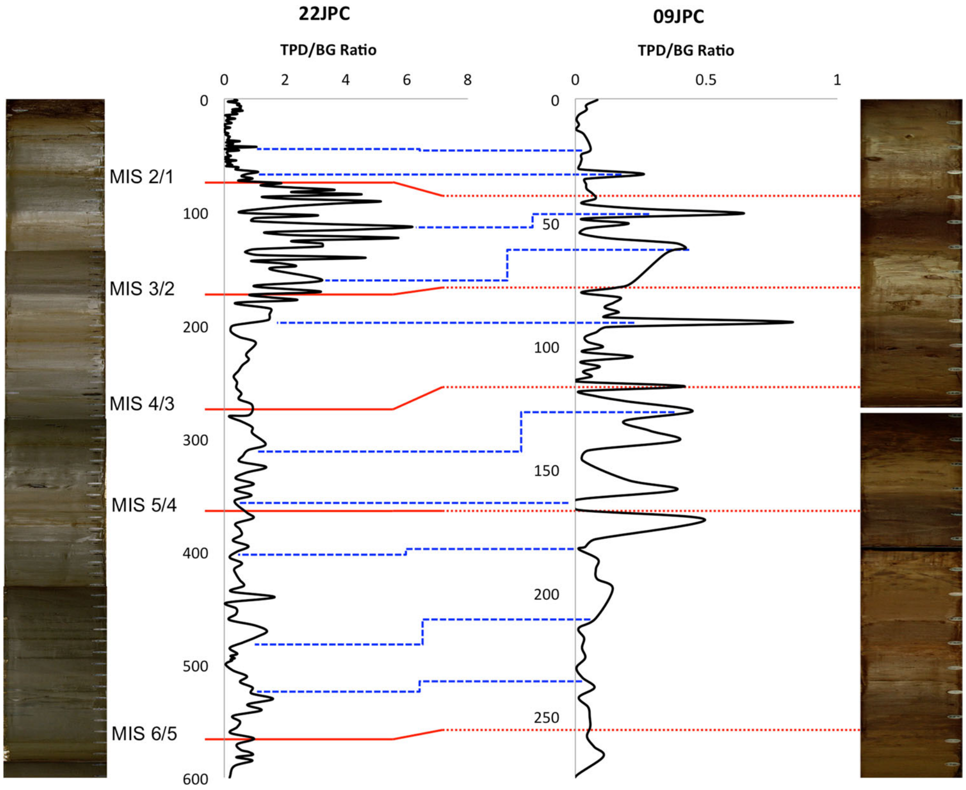

Fig. 4 TPD/BG ratio plotted against depth for both 22JPC and 9JPC. The MIS indicated for 22JPC records (*solid red line*) and depth of MIS for 9JPC are estimated (*dotted red line*). These estimated depths were used to derive initial index correlation points, which are indicated with the *dashed blue lines*

Additionally, illite, illite/smectite mixed-layered clays, kaolinite, and chlorite were included as these clay minerals show strong temporal variation, whereas other mineral phases do not (Fig. 6). Occasionally, due to sampling differences, a direct depth match was not available in the 22JPC and/or the 9JPC mineralogy, and in these cases the trend between the adjacent samples was used to test the correlations. The mineralogy was never an exact match, due to the core site locations receiving varying amounts of mineral inputs due to source proximity. For example, 9JPC will receive more plagioclase and smectite due to the proximity to dominant sources of these minerals.

Due to the difference in the bottom water conditions at the 9JPC and 22JPC core sites, many of the elements commonly used in chemostratigraphy cannot be utilized in this study. In many studies, Mn is shown to be a very useful tool for correlation. However, given the distance between the two core sites in this study and the difference in bottom water conditions, highly reactive elements such as Mn and Fe do not appear to be very useful as direct correlation markers. Manganese is delivered to the Arctic through riverine input [46], so these Mn layers will be more prominent in the central portion of the Arctic [29]. Core 22JPC, however, is situated far from the river mouths and its sediments are not as enriched in Mn. Additionally, both Mn and Fe are mobilized in marine sediments through bioturbation [44]. 22JPC is under Arctic to sub-Arctic conditions and therefore likely experiences higher degrees of bioturbation. Due to this mobilization, the Mn and Fe signals in 22JPC will appear to be different from the correlated layer in 9JPC.

The elements Ca and Ba are intimately linked to marine biologic productivity [47]. Due to the greater biogenic production and better preservation at core site 22JPC relative to 9JPC, these biologically linked elements are not very useful. Localized inputs of Svalbard dolomite to 22JPC also add to the difficulty in using the Ca signal as a correlation marker. Other analyzed elements in this study are too close to detection limits to express the variability needed to produce viable correlations. Therefore, the geochemical signatures that are not easily mobilized (labile) through biologic activity and have values sufficiently above detection limits with variability suited for correlation are K, Ti, Co, Rb, and As (Fig. 7).

Correlation

Beginning with the TPD/BG ratio, 10 peaks/troughs were identified as initial correlation picks that could be used to transfer the age model from 22JPC (bold values in Table 2, marked in Fig. 4). For each potential correlation pick, if two of the three primary mineral phases and two of the four additional minerals matched (gray bars; Fig. 6), the pick was confirmed and the geochemistry (bulk XRF analyses) was then examined to further confirm and/or refine these correlations (gray bars; Fig. 7). If the majority of the

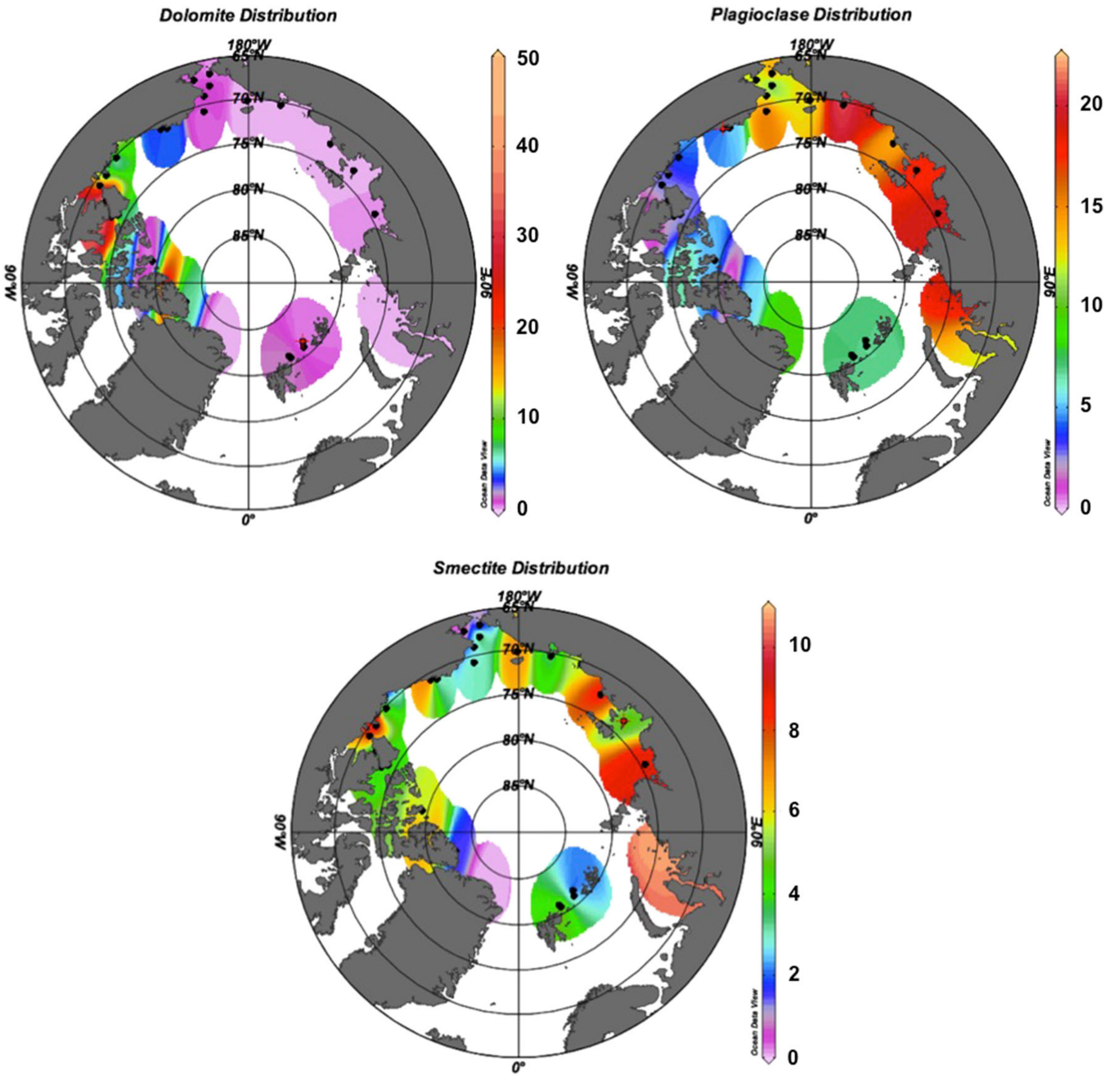

Dolomite Distribution

Plagioclase Distribution

Smectite Distribution

Fig. 5 Mineral distribution plots of the three identified primary minerals. Quantitative bulk mineralogy determined using RockJock software [26]. *Black dots* indicate sample locations. Dolomite is sourced exclusively to the Banks and Victoria Island region of Canada. Plagioclase is almost exclusively sourced to the Laptev and East Siberian Seas. The smectite signal is strongest in the Kara and western Laptev Seas. The *color scales* represent the percentage for the mineral distributions. Plots created with Ocean Data Viewer with weighted-average grid interpolation [55]

geochemical elements match, then the pick is considered a match and is used as a correlation point. Forty-one such points were identified through this method and were used in the age model interpolation of 9JPC (Table 2).

The 9JPC age model was calculated using PCHIP (Fig. 8). The 9JPC record encompasses ~140 kyrs, with an overall average sedimentation rate of 1.9 cm kyr^{-1} ($R^2 = 0.985$) calculated by the linear fit, but this core exhibits a high variability (Fig. 8). All major shifts in sedimentation are analyzed by a linear fit over the interval in question; sedimentation rates are determined from the slopes and the correlation coefficients are based on the degree of fit.

MIS sedimentation rates

The variations in sedimentation rate generally fit well within the expected glacial ice-rafting history of the region (Figs. 8, 9). In 9JPC, the average sedimentation rate for MIS 5 to the present is 2.0 cm kyr^{-1} ($R^2 = 0.990$). This average sedimentation rate is comparable to that of a nearby core HLY0503-8JPC on the Mendeleev Ridge where a 2 cm kyr^{-1} rate was recorded for MIS 5 to present [2].

Comparisons to previously published data for dated central Arctic sediment cores show that in general, the rates found in this study compare well to published sedimentary

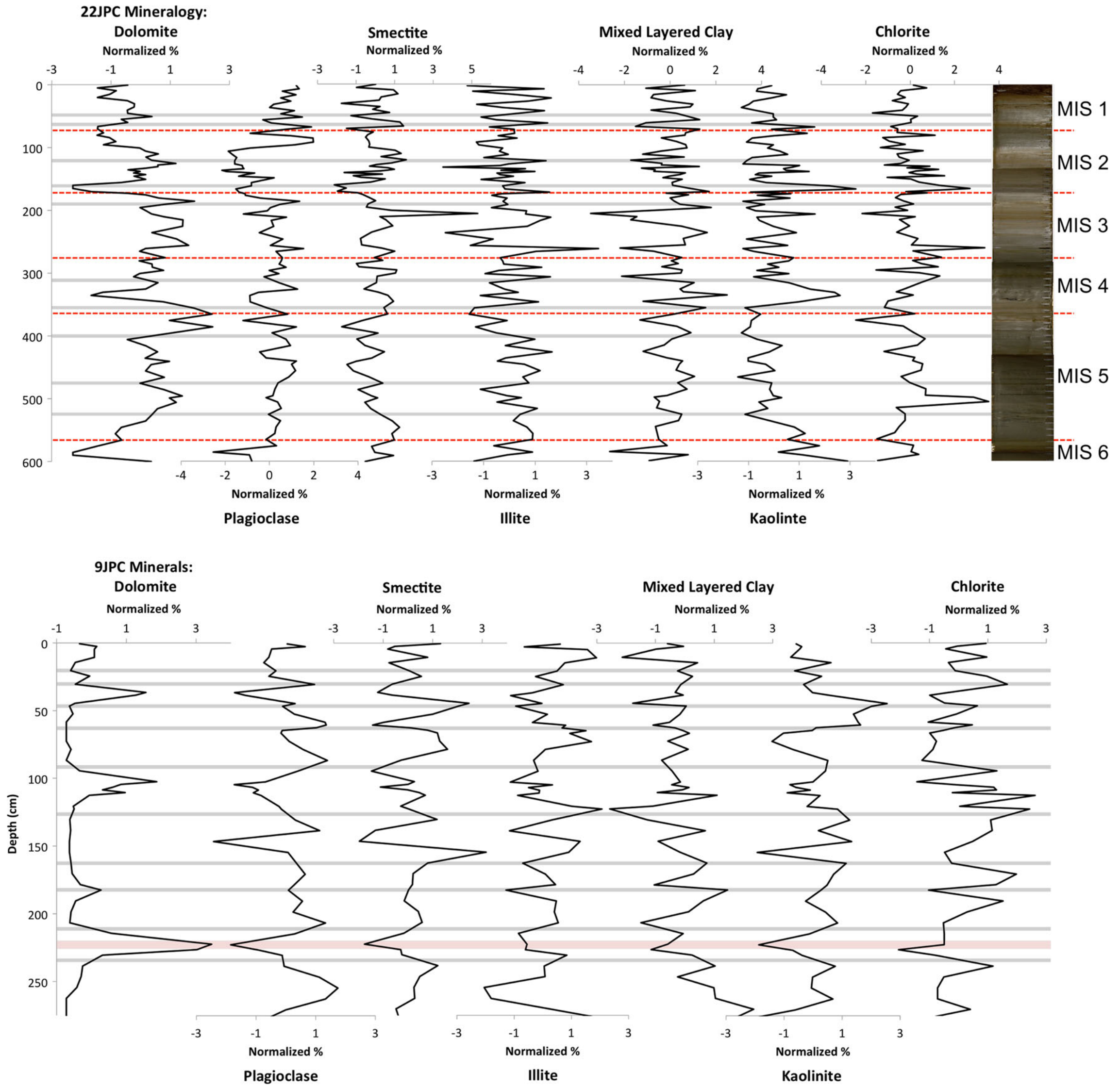

Fig. 6 Quantitative bulk mineralogy of the <45-µm fraction for 22JPC and 9JPC. *Gray bars* highlight the index picks as determined from the TPD/BG ratio. Data were normalized by variance to better visualize the shift about the mean (0). PW2 is identified through identification of increased grain size, enhanced dolomite deposition, and the pink hue of the core. PW2 occurs in MIS 5d (107 ka; [62]) but is not used in the correlation; instead the timing of this event is used as an independent test for the age model

rates for central Arctic sediment records [41]. In this study, due to rapid sedimentation events the sedimentation rates during Stages 2–4 are slightly higher than the given ranges of Levitan and Stein [41].

Sedimentation during MIS 6 to MIS 1

Only part of MIS 6 is covered by the correlated age dates in 9JPC and these only cover the youngest part of this stage, but a period of elevated sedimentation occurs for this core at ca. 139 ka with a rate in excess of 16 cm kyr^{-1} (Fig. 8; E8 in Fig. 10). Following this event the rate falls to 0.8 cm kyr^{-1} as Stage 6 transitions into Stage 5. The partially recovered rapid accumulation event of Stage 6 reveals high sedimentation rates that would be indicative of the high ice floes associated with deglaciation and the transition from a glacial maximum, which is tentatively dated at ca. 140 ka [33, 65]. The lithology confirms that there is a sharp increase in mean grain size, indicating an increase in IRD (Fig. 9). The Mn signal at this time exhibits a low that is immediately followed by a sharp increase, indicating that either Mn was not being delivered to the system or being oxidized until after a major ice sheet disintegration event [29, 45]. A small jump in both dolomite and smectite is found to occur at this time, which coupled with the increased grain size suggests ice rafting from both

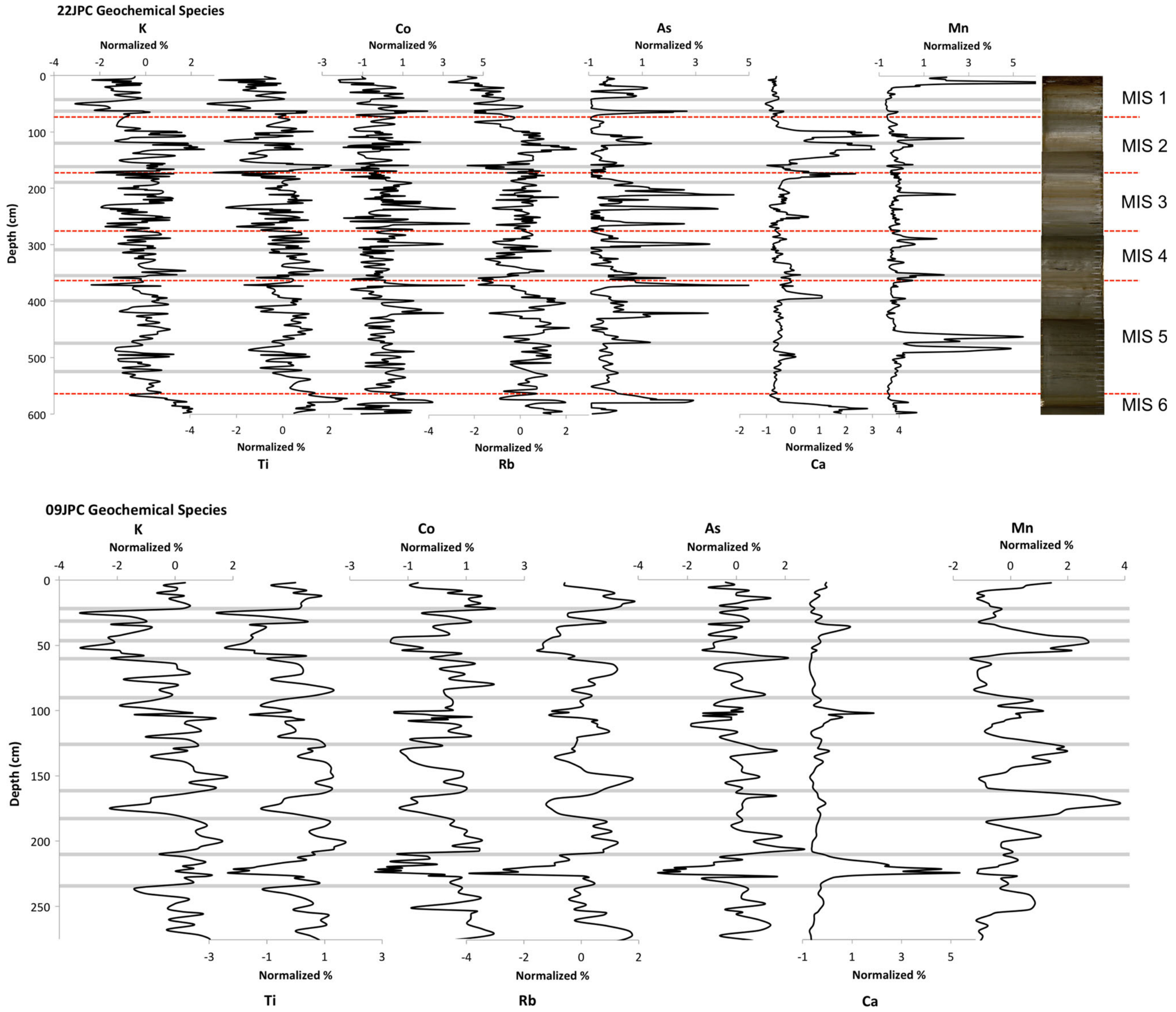

Fig. 7 Bulk XRF data for 22JPC and 9JPC. *Gray bars* highlight the index picks as determined from the TPD/BG ratio. Again, data were normalized by variance to better visualize the shift about the mean (0)

the North American and Eurasian Ice Sheets [22, 66]. The average sedimentation for the period of ca. 140–130 ka of 1.8 cm kyr^{-1}, interspersed with a short period of >15 cm kyr^{-1} in 9JPC, is what might be expected for a period of intermittent iceberg discharges to an interglacial period with even larger discharges of glacial ice during the initial stages of warming. Because our analysis does not extend into MIS7, we cannot be certain as to the base of MIS6.

MIS 5 exhibits highly variable rates of sedimentation ranging from <1 cm kyr^{-1} in early Stage 5 to >8 cm kyr^{-1} at ca. 76 ka with an overall average of 1.6 cm kyr^{-1} ($R^2 = 0.981$) based on the linear trend across the full stage (Fig. 8). The plot of MIS 5 age model indicates that there are a number of distinct changes in sedimentation rate (Fig. 8; Table 2), some of which correspond to the MIS 5 substages. Early in Stage 5 from 130 to 114 ka and encompassing substage 5e, the sedimentation rate was quite low at 0.7 cm kyr^{-1}. From ca. 114 to 97 ka the sedimentation increases to a rate of 1.7 cm kyr^{-1} ($R^2 = 0.997$) and then further increases to 2.3 cm kyr^{-1} ($R^2 = 0.987$) between 97 and 91 ka. These two periods constrain both substages 5d and 5c, which peak at 109 and 96 ka, respectively, and imply increasing rates of sedimentation through this time. At around 89 ka there is a decrease in sedimentation to a minimum of 0.7 cm kyr^{-1} ($R^2 = 0.992$) that persists for approximately 11 kyrs, and encompasses substages 5b and 5a. Following this quiescent period, a sharp increase in sedimentation occurs at ca. 77 ka for approximately 500 years reaching a rate in

Table 2 Correlation picks for the 9JPC to 22JPC age model transfer

Marine isotope stage	HIY0503-9JPC depth (cm)	HLY0503-22JP C depth (cm)	Age from LR04-22JPC age model (kyr)	9JPC sedimentation rate (cm kyr^{-1})	22JPC sedimentation rate (cm kyr^{-1})
MIS1	2.5	12.5	2.5	1.0	5.0
	14.5	30.5	5.8	3.6	5.5
	20.5	**42.5**	**8.3**	**2.4**	**4.8**
	25.0	50.0	9.9	2.8	4.7
	28.5	59.5	11.9	1.8	4.8
	30.5	**64.5**	**12.9**	**2.0**	**5.0**
	Average rate from linear fit (R^2)			**2.7** (0.981)	**5** (0.999)
MIS 2	32.5	72.5	14.3	1.4	5.7
	40.5	90.5	16.9	3.1	6.9
	44.5	110.5	18.1	3.3	16.7
	46.5	**120.5**	**19.0**	**2.2**	**11.1**
	55.5	138.0	21.4	3.8	7.4
	Average rate from linear fit (R^2)			**2.7** (0.970)	**8** (0.944)
MIS 3	**60.5**	**160.0**	**25.5**	**1.2**	**5.3**
	64.5	165.5	26.9	2.9	3.9
	72.0	167.0	27.3	18.7	3.7
	74.5	170.5	28.5	2.1	2.9
	76.5	173.0	29.6	1.8	2.3
	78.5	180.5	33.1	06	2.1
	86.5	185.5	35.4	3.5	2.2
	90.5	**190.5**	**37.2**	**2.2**	**2.8**
	96.5	203.0	38.4	5.0	10.4
	100.5	213.0	38.8	10.0	25.0
	102.5	225.5	42.6	0.5	3.3
	103.0	234.0	46.2	0.1	2.4
	108.5	258.0	53.5	0.8	3.3
	114.5	265.5	54.0	12.0	15.0
	Average rate from linear fit (R^2)			**1.3** (0.876)	**3.8** (0.976)
MIS 4	120.5	285.5	62.6	0.7	2.3
	126.5	**310.5**	**63.5**	**6.7**	**27.8**
	130.5	320.5	63.9	10.0	25.0
	142.5	325.5	64.2	40.0	16.7
	154.4	350.5	67.1	4.1	8.6
	162.5	**355.5**	**68.3**	**6.7**	**4.2**
	Average rate from linear fit (R^2)			**6.1** (0.901)	**13.6** (0.900)
MIS 5	170.5	380.5	75.8	1.1	3.3
	178.5	390.5	76.6	10.0	12.5
	182.5	**400.5**	**82.6**	**0.7**	**1.7**
	190.5	445.5	91.3	09	5.2
	210.5	**475.5**	**99.7**	**2.4**	**3.6**
	222.5	498.5	107.1	1.6	3.1
	230.5	515.5	111.5	1.8	3.9
	234.5	**525.5**	**113.4**	**2.1**	**5.3**
	Average rate from linear fit (R^2)			**1.6** (0.981)	**3.8** (0.995)
MIS 6	254.5	575.5	139.3	0.8	1.9
	266.5	577.5	159.9	20.0	3.3
	Average rate from linear fit (R^2)			**NA**	**NA**

Bold rows indicate the initial picks based on the TPD/BG ratio. The sedimentation rates for 9JPC and 22JPC are calculated for each interval for comparison. The sedimentation rate for each MIS is given and based on the linear fit for each interval excess of 8 cm kyr^{-1}. After this fairly rapid event, the sedimentation rate falls <1 cm kyr^{-1} as Stage 5 transitions into Stage 4.

The average Stage 5 sedimentation rates from this study for the Mendeleev Ridge along the margins of the East Siberian Sea can be in excess of 5 cm kyr^{-1} [41, 62]. Based on sedimentation rate distribution maps for the region of the Mendeleev Ridge, 9JPC is located in a 1–5 cm kyr^{-1} band [41], which corresponds with the 1.6 cm kyr^{-1} calculated average rate in this study. The lower sedimentation rate seen in 9JPC, relative to the rates found along a southern transect of the Mendeleev ridge [62], can be attributed to the core location. The farther the core site is from the continental margin, the less the sediment that core will generally receive, as the proximity to the source exerts an important control on sedimentation [33]. Overall, the large variability in sedimentation identified for MIS 5 is to be expected for a long-term interglacial period with well-documented fluctuations in global ice volume during stadials.

The variability of sedimentation rates calculated for the MIS 5 substages fit nicely into the model of MIS 5 environmental changes. Substage 5e, a warm interval, shows a decrease in the rate of sediment accumulation from the already low rate of sedimentation at MIS 6/5 transition, probably due to less ice-rafting, as the textural data indicate that >97 % of this material is <63 µm through this period (Fig. 11). As the global climate system transitioned to a stadial (substage 5d), the associated lower temperatures allowed for increased sea ice production and potentially glacial ice rafting. This is suggested by textural data where >63 µm material increases in 9JPC from <2 to ~9 % (Fig. 11). This increase in coarse IRD corresponds to an increase in sedimentation for the region.

Pink/white (PW) coarse layers were initially identified as correlation markers [9]. These layers were later discovered to be somewhat problematic because the number of these layers was not always the same in relatively nearby cores [16, 29, 54, 62]. Because these PW layers can only be correlated by their sequence in cores and no unique mineralogy or chemistry can distinguish corresponding PW layers, we did not use them in the correlation. However, the identification of PW2 at ~107 ka does provide somewhat of a confirmation of the age model (Fig. 9). PW2 is contemporaneous with the widely accepted age for this event, Stage 5d [62].

Substage 5c is associated with a continuing increase in sedimentation rate, possibly related to freshwater event 5.4. This event has previously been identified in a Mendeleev record to occur in substage 5d [51]. This difference in timing could indicate that the age model in this study or that used by Polyak et al. [51] is slightly off during mid-MIS 5. Stadial 5b follows with a decrease in sedimentation rate. This substage is associated with increased glacial rafting as evidenced by the large jump in the >250 µm fraction (up to ~7.5 %; Fig. 11). The sea ice entrainment and transport are likely reduced as a result of the increased terrestrial ice volume of the Arctic during this time and the restriction in entrainment zones (i.e., exposed shelves). As the 9JPC transitions into substage 5a, the overall climate is cooling as the climate system begins to transition to the MIS 4 stadial. There is an overall increase in sedimentation during this time. This increase is substantiated by the increase in >63 µm fraction and subtle decrease in >250 µm, which suggests perhaps a stronger sea ice signal than seen in the previous stadial (5b) (Fig. 11). Lithologically, Stage 5 exhibits variability consistent with the stadial/interstadial changes (Figs. 9, 11, 12). During interstadial periods (5e, 5c, and 5a), levels of smectite are elevated while dolomite is low. This implies a period where ice sheets are small or missing and sea ice transport dominates. The largest sea ice entrainment regions are the broad shelves of the East Siberian and Laptev Seas, which is dominated by a smectite signal from the Siberian Trap Basalts [22, 66, 68]. These findings confirm that changes in sedimentation in the Arctic Ocean are strongly linked to the mode of ice rafting (glacial vs. sea ice).

Stage 4 exhibits a high average sedimentation rate of 6.1 cm kyr^{-1} ($R^2 = 0.901$), but also exhibits a wide range of rates from <1 cm kyr^{-1} at the 5/4 and 4/3 transitions to a maximum of >20 cm kyr^{-1} for a short period at ca. 64 ka. This variability can be seen in the age model, with three distinct periods of low sedimentation separated by rapid accumulation events (Figs. 8, 10). Around 64 ka a large sustained increase in terrestrial ice volume might have occurred, which is followed by the maximum sedimentation during this stage of 23 cm kyr^{-1} ($R^2 = 0.974$), lasting for approximately 500 years. From this maximum sedimentation, the rates gradually decline until the Stage 4/3 transition. The period of 63–60 ka exhibits a rate of 1.2 cm kyr^{-1} ($R^2 = 0.982$), followed by a further reduction to 0.6 cm kyr^{-1} ($R^2 = 0.982$) at the Stage 4/3 transition.

Stage 4 is unique in that it is a somewhat warm stadial. Thus, ice sheet thickness and extent are not as great during this time as it were during other glacial stages [40, 65]. The

Fig. 8 *Upper* 9JPC interpolated age model with core photo. MIS are identified (*red lines*). Note the distinctive sedimentation rate variability and the numerous rapid sedimentation events that occur throughout. Linear fit of the curve provides the overall average sedimentation rate of 1.9 cm/kyr. Interpolation is based on the sampling resolution of the Fe grain provenance. *Lower* 9JPC interpolated age models for Stages 1–5 and a portion of Stage 6. As with this figure, again the interpolation is based on the sampling resolution of the Fe grain provenance ▶

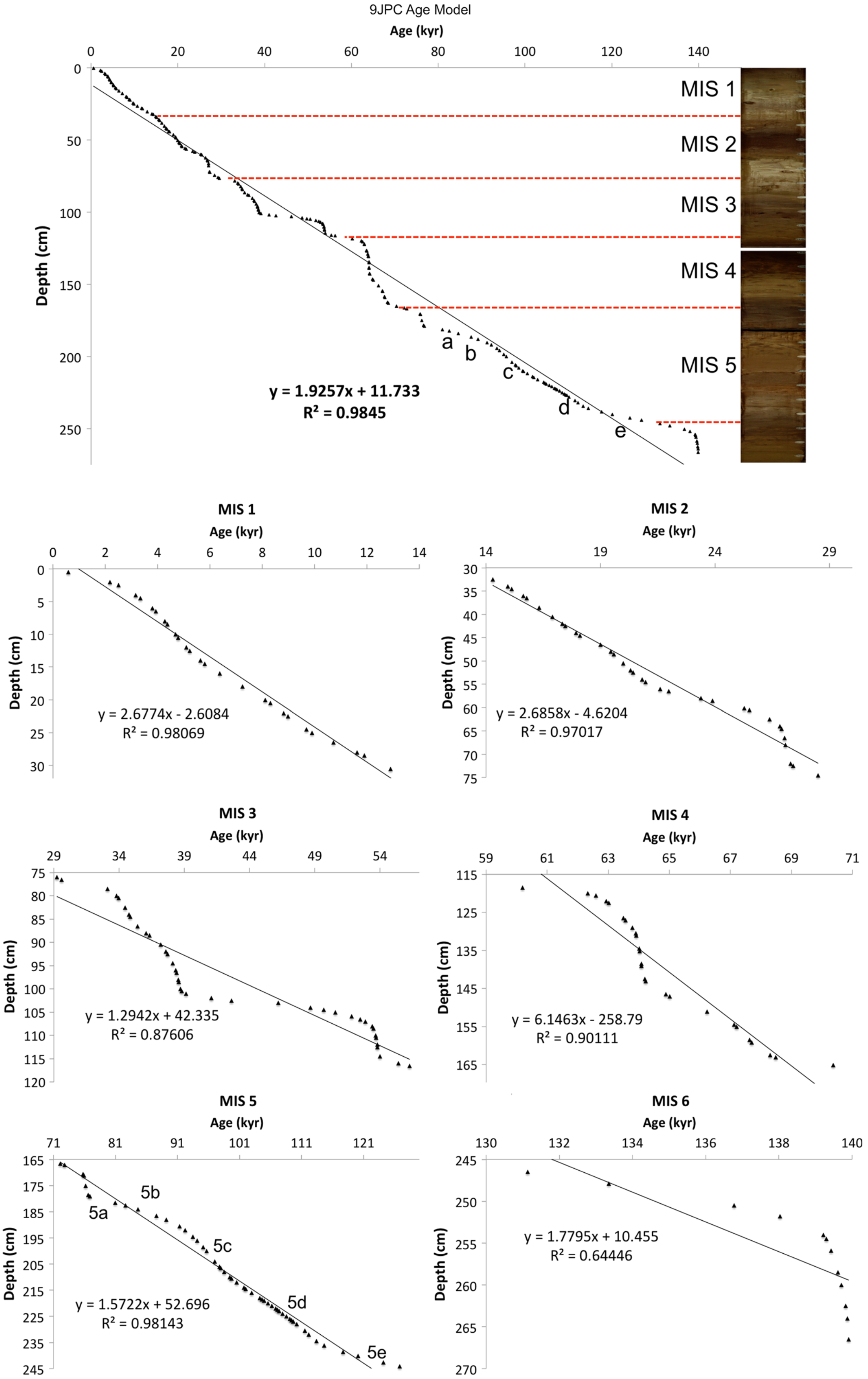
9JPC Age Model
Age (kyr)
0
20
40
60
80
100
120
140
Depth (cm)
0
50
100
150
200
250
MIS 1
MIS 2
MIS 3
MIS 4
MIS 5
a
b
c
d
e
y = 1.9257x + 11.733
R² = 0.9845
MIS 1
Age (kyr)
0
2
4
6
8
10
12
14
Depth (cm)
0
5
10
15
20
25
30
y = 2.6774x - 2.6084
R² = 0.98069
MIS 2
Age (kyr)
14
19
24
29
Depth (cm)
30
35
40
45
50
55
60
65
70
75
y = 2.6858x - 4.6204
R² = 0.97017
MIS 3
Age (kyr)
29
34
39
44
49
54
Depth (cm)
75
80
85
90
95
100
105
110
115
120
y = 1.2942x + 42.335
R² = 0.87606
MIS 4
Age (kyr)
59
61
63
65
67
69
71
Depth (cm)
115
125
135
145
155
165
y = 6.1463x - 258.79
R² = 0.90111
MIS 5
Age (kyr)
71
81
91
101
111
121
Depth (cm)
165
175
185
195
205
215
225
235
245
5a
5b
5c
5d
5e
y = 1.5722x + 52.696
R² = 0.98143
MIS 6
Age (kyr)
130
132
134
136
138
140
Depth (cm)
245
250
255
260
265
270
y = 1.7795x + 10.455
R² = 0.64446

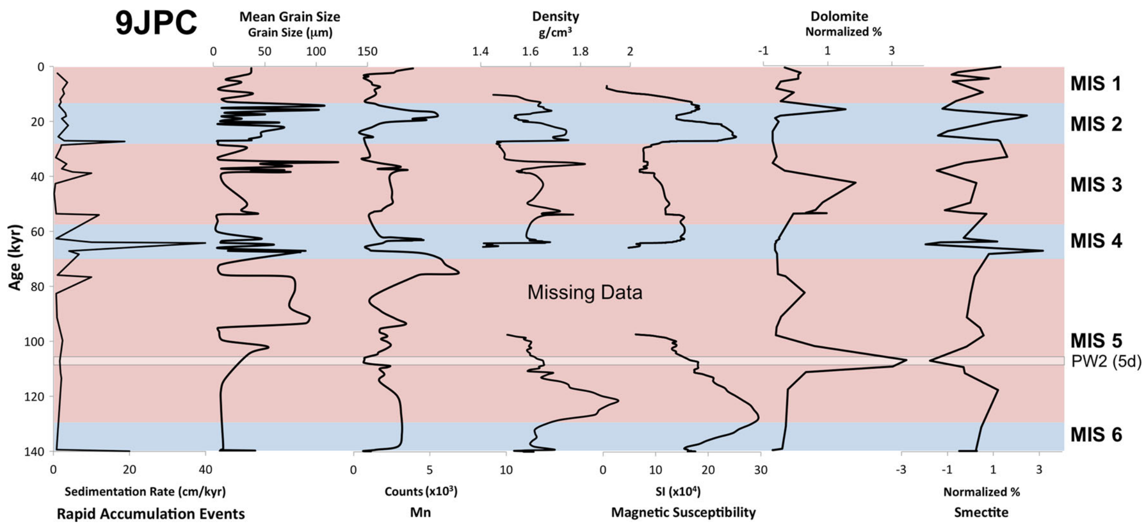

Fig. 9 Summary figure of 9JPC lithostratigraphy incorporated with the age model. Mean grain size, Mn variability, sediment density, magnetic susceptibility, and dolomite and smectite variations are shown. The MIS boundaries are indicated and each stage is *color coded* to depict the general climatology (*red*-warm and *blue*-cool). Although not used to test correlations, a probable *pink*/*white* layer, PW2, is shown. The model places this event in Stage 5d, consistent with the accepted age [62]

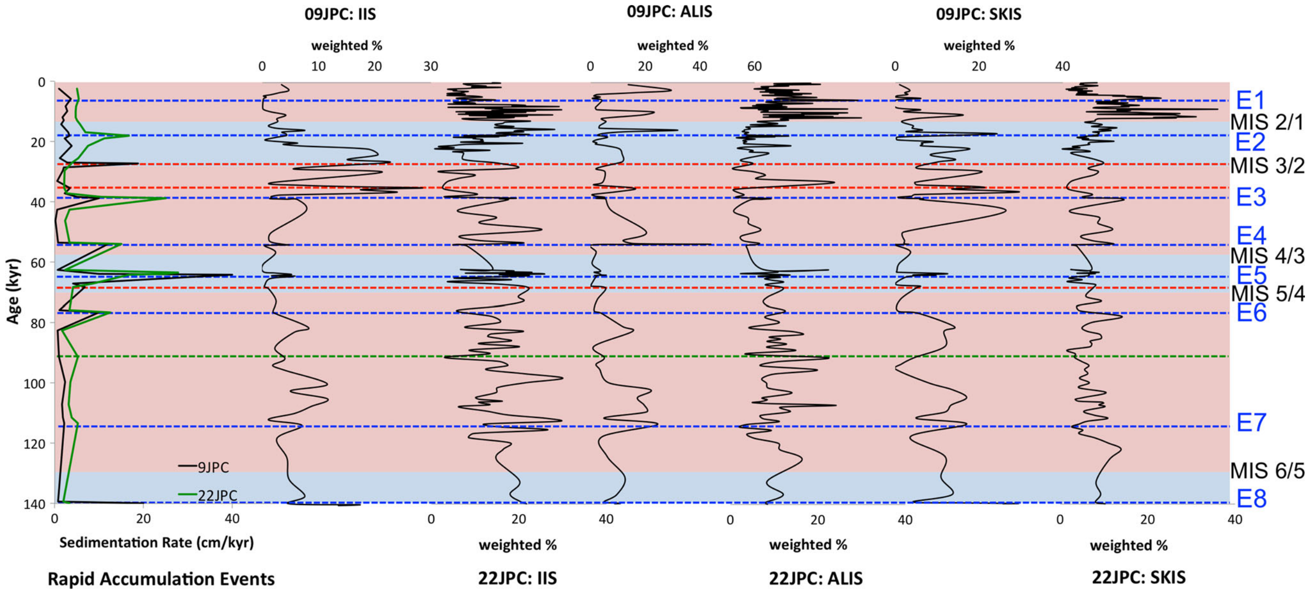

Fig. 10 Sedimentation rate variability (*left plot*) for 22JPC (*green*) and 9JPC (*black*) based on linear sedimentation rates, with MIS periods highlighted. Fe grain source matches are shown for 22JPC and 9JPC for the Arctic Laurentian Ice Sheet group (ALIS), Innuitian Ice Sheet group (IIS), and the Svalbard/Kara Ice Sheet group (SKIS). Highlighted on the plots are basin-wide events (*blue dashed line*; and labeled E1-E8), 22JPC-specific events (*green dashed line*), and 9JPC specific events (*red dashed line*)

result of these stadial-like conditions might be unstable ice sheets that result in regular massive iceberg discharges or freshwater events. This is seen in the record of highly variable sedimentation rate during this stage. The >250 µm textural data indicate two periods of massive iceberg discharge at ca. 64 and 63 ka (Fig. 11). The placement of these two events is slightly offset from the rapid sedimentation event that the age model indicates. Stage 4 exhibits a high variability in grain size, Mn, and smectite contents (Figs. 9, 11, 12) that is indicative of a period that is climatically unstable.

The relatively low sedimentation rate associated with the MIS 4/3 transition becomes slightly elevated at the beginning of Stage 3. This period is sharply interrupted by a short (~750 years), but major sedimentation event at ca. 54 ka with a rate of sedimentation of >14 cm kyr^{-1}. The

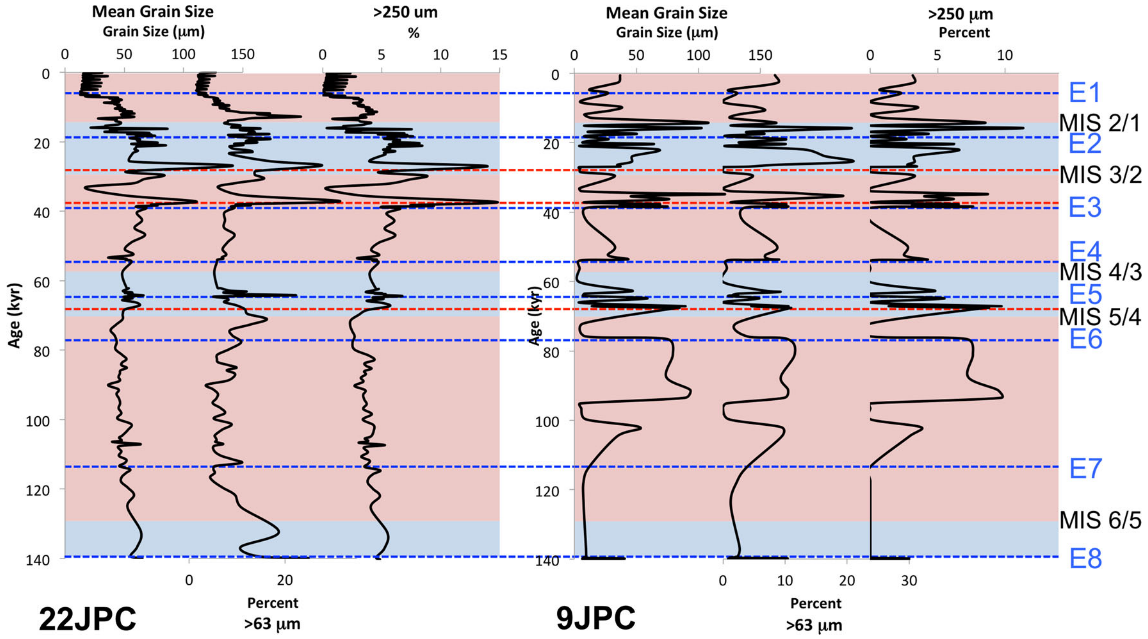

Fig. 11 Texural data (mean grain size, >63, and >250 µm) plotted for 22JPC (*left*) and 9JPC (*right*). MIS boundaries are marked with *black dashed lines*; major accumulation events highlighted in Fig. 10 are also highlighted here

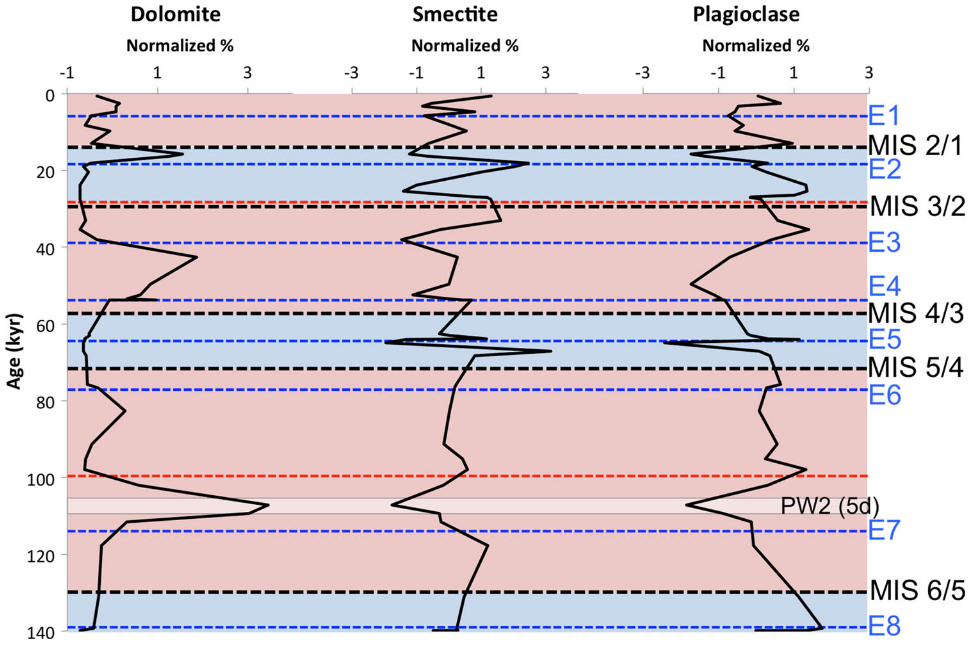

Fig. 12 9JPC Primary minerals (% normalized by variance) plotted against age. The rapid accumulation events are highlighted as done in Fig. 10. The probable *pink*/*white* layer, PW2, is indicated

following interval of 52–39 ka is associated with low, <1 cm kyr^{-1} sedimentation. Around 39 ka, >6 cm of sediment was deposited very rapidly in roughly 500 years. This corresponds to a rate of nearly 14 cm kyr^{-1}. Following this pulse of sediment, a rate of 3 cm kyr^{-1} occurs for the next four to five millennia. From 33 ka through the Stage 3/2 transition, the sedimentation rate falls again to <1 cm kyr^{-1}.

Stage 3 is a cool interglacial and is interspersed with interstadial to stadial-like conditions [40, 65]. The result of this cooler environment is that terrestrial ice is still likely an influence in the sedimentation history during this time. The lithological and textural data indeed imply that glacial ice is present as this period is associated with a few rapid increases in the mean grain size tied to the >250-µm fraction and large swings in sediment density and dolomite concentration (Figs. 9, 11). For this region of the Mendeleev Ridge, sedimentation rate distribution maps imply a <1 cm kyr^{-1} signal [41]. The average estimated rate from this study is 1.3 cm kyr^{-1}, which is slightly higher than the Levitan and Stein [41] estimates due to the inputs of glacial ice and/or large-scale sea ice entrainment events.

Early in Stage 2 there is approximately 500 years of rapid sedimentation at around 27 ka, amounting to a rate of >8 cm kyr^{-1}. After this event sedimentation decreases to 1.4 cm kyr^{-1} and remains unchanged for the next 5 kyr. At ca. 22 ka, the sedimentation rate increases to approximately 3.3 cm kyr^{-1} and continues with minimal variation until the Stage 2/1 transition (Fig. 9).

Sedimentation during the LGM was reduced in the central Arctic and contains very fine-grained material or results in a hiatus of several thousand years for this region of the Mendeleev Ridge [53], but this is not a consistent feature across the entire central Arctic [33]. Additionally, just prior to and after the LGM the IRD in the western Arctic cores consists of sediment most similar to that from the Mackenzie River region [53]. This implies that the material during this time is sourced to glacial erosion from the Laurentide ice sheet as it reached its maximum extent when the sea level was at its lowest. The mineralogy data from this study show elevated dolomite between 23 and 25 ka and a sharp increase in dolomite at $\sim$16 ka in core 9JPC (Fig. 12), which seems to substantiate this Laurentide source due to the abundance of dolomite on Victoria Island and adjacent areas eroded by this ice sheet [53]. The lithology of 9JPC shows that early in MIS 2 a large increase in mean grain size occurs until ca. 20 ka, potentially representing the rapid growth of terrestrial ice sheets and the associated pulse of coarse IRD.

The Holocene exhibits some minor variability, though not as much as previous interglacials/interstadials. The overall average sedimentation rate for this period in 9JPC is calculated to be 2.7 cm kyr^{-1} ($R^2 = 0.981$). The maximum sedimentation rate for Stage 1 occurs at approximately 6 ka and reaches accumulation in excess of 4 cm kyr^{-1}, persisting for approximately 1.5 ka. The rate steadily declines reaching a minimum of approximately 1.3 cm kyr^{-1} at ca. 3 ka and continues at this rate until present day. Based on the lithology, the Holocene period is associated with minor variation in sediment grain size, dolomite and smectite content, and an initial pulse in Mn followed by a steady increase (Fig. 9). These three features would be indicative of an ocean with primarily sea ice-rafting from both North American and Eurasian sources and increasing riverine inputs.

Rapid sediment accumulation events

The age model presented here identifies eight periods of rapid sedimentation in MIS 6 to MIS 1 that were recognized in both 9JPC and 22JPC (Fig. 10). When these events are synchronous in both 22JPC and 9JPC, it implies that basin-scale processes govern these rapid mass accumulation events. If only identified in 9JPC or 22JPC, then it is likely that localized processes such as a local melt-out event or local sea ice entrainment event account for the rapid accumulation. Thus, the widespread occurrence of these rapid events is likely linked to terrestrial ice dynamics such as a major glacial lake outburst, the disintegration of ice sheets following a glacial maximum, or for warm intervals, episodes of increased sea ice entrainment.

For the most part, the timings of these rapid accumulation events correspond well with documented glacial activity. The late Pleistocene history of Eurasian glaciation is well understood, and major ice sheet advances have been documented for MIS 6, 5b, Stage 5/4 and 4/3 transitions, and the LGM [38, 59, 65]. North American glaciations are documented to have occurred during MIS 6, MIS 5d, at the transition from MIS 4 to 3, and the LGM [20, 51], but this history is still only partially understood [33, 35, 52, 62]. By examining the matched sources of Fe grains for the rapid deposits identified in this study, it is possible to identify where the signal originates and potentially show the relationship between the Eurasian and North American ice sheet calving for glacial periods [16] and distinguish major regions of sea ice entrainment during interglacials. The Innuitian Ice Sheet (IIS) signal is the combined source matches that correspond to the source areas labeled in Fig. 3 that encompass the northern and southern Queen Elizabeth Islands: source areas 2, 3, 4, 5, 6, 7, 24, 25, 26, and 28 [16]. The Arctic Laurentide Ice Sheet (ALIS) consists of the western Canadian Arctic Archipelago and northern Alaska, including the Mackenzie River. The sources for the ALIS are source areas 8, 9, and 10 (Fig. 3). The Svalbard-Kara Ice Sheet (SKIS) sources consist of the sources in the Barents and Kara Seas, represented by source groups: 12, 14, 15, 16, 29, 30, 31, 32, 33, and 36 (Fig. 3).

There is a distinct jump in sedimentation rate upwards of 20 cm kyr^{-1} at ca. 139 ka, Event 8 (E8, Fig. 10). The timing of this event is close to the estimated Stage 6 glacial maximum of ca. 140 ka [65] and might represent the disintegration of Stage 6 ice sheets. This period does correspond to a freshwater event identified by isotopic lows across multiple Arctic records that range from 140 to 125 ka and is interpreted to be the release of an ice-dammed lake(s) from the Eurasian ice sheets [59]. The Fe grain matches and mineralogy, however, indicate that there is an additional North American source for this event. The mineralogy of this event does show a Laptev Sea source, as there is a large increase in the plagioclase signal that indicates a strong Eurasian input for 9JPC (Fig. 12). Both dolomite and smectite phases show a very small increase at ca. 139 ka (Fig. 12), which indicates that the Laurentide Ice Sheet and the Kara and Yenisey River sources are of minimal importance during this period of accumulation in late Stage 6. The Fe grain provenance, however, shows a strong increase in IIS and SKIS sources and ALIS to a lesser degree in 9JPC, while in 22JPC the three source regions are only slightly elevated (Fig. 10). The texture of the sediment at this time also shows evidence of a large increase in ice transport (both sea ice and glacial ice) as the >63 and >250 μm fractions increase to >10 and 3 %, respectively (Fig. 11). Thus, if it is determined that this accumulation event corresponds with the Stage 6 freshwater event [59], then this freshwater event cannot be sole sourced to the Eurasian Ice Sheet but a North American component must also be contributing. Isotopic evidence would be necessary to confirm that these two events are the same.

In Stage 5, two events were identified in both 9JPC and 22JPC (E7 and E6; Fig. 10). In 22JPC for E7, a rate of 5.3 cm kyr^{-1} is recorded at ca. 113 ka, with no appreciable source increase in IIS, ALIS, or SKIS. At ca. 111.5 ka, the sedimentation rate in 9JPC increases to 3.9 cm kyr^{-1} and is associated with an increase in each major ice sheet source (Fig. 10). The grain size indicates that iceberg transport is likely the dominant transport mechanism for this event, given that the texture of the >63 and >250 μm both show distinct jumps (Fig. 11). Interestingly, this period occurs prior to the beginning of PW2 (dated at ~107 ka in this study). Following this rapid event and transitioning into the PW layer, the >63 μm fraction increases to >10 % and the contribution from the ALIS shows a sharp increase (Figs. 10, 11). The offset between the timing of the rapid event in 22JPC and 9JPC might indicate signal lag, where IIS, ALIS, or SKIS calving occurs earlier than the others. Higher-resolution records are likely needed to determine the timing of these potential lags.

The second Stage 5 event, E6, occurred at approximately 77 ka (Fig. 10). In 22JPC and 9JPC, sedimentation rates increased to 12.5 and 10 cm kyr^{-1}, respectively. These rates are roughly 3 and 5 times that of the average rates during this period. This period potentially corresponds to a 77 ka melt water signal found in a series of cores along the TPD through the Fram Strait [36]. This freshwater signal was determined to originate from ice-dammed lakes from northern Siberia, given the strong smectite signal that is indicative of the Siberian Trap Basalts [36]. The Fe grain source data show that there in an increase in SKIS, ALIS, and IIS here (Fig. 10). The grain-size data for 9JPC indicate an ice transport source for this rapid event, with >63 μm exceeding 10 %. Fe grain provenance data for E6 indicate that all ice sheet sources are on the decline in 9JPC.

At 64 ka rapid event E5 occurred, resulting in the highest sedimentation rates determined to be ~40 and ~28 cm kyr^{-1} for 22JPC and 9JPC, respectively (Fig. 10). After application of the age model, this ~40 cm kyr^{-1} rate corresponds to a time in which 16 cm of sediment is deposited in <1 kyr. Thus, the rate is really >20 cm kyr^{-1}. In 9JPC, this event is associated with sharp increases in both smectite and plagioclase that indicates a strong Eurasian source (Fig. 12). Indeed, the Fe grain provenance shows an increase in source material from SKIS as well as IIS and to a lesser degree ALIS, with similar provenance found in 22JPC (Fig. 10). With a >250 μm fraction more than 5 % (Fig. 11), this event may correspond to an IRD event from between late Stage 4 and early Stage 3 (65–50 ka) identified as a thick IRD-rich layer found throughout the Arctic [29, 59, 67]. This layer is commonly associated with high levels of smectite and kaolinite [66], which suggests an SKIS source. In 9JPC and 22JPC, Fe grain provenance shows an increase in SKIS sources but also increases in IIS sources and small increases in ALIS (Fig. 10). This suggests that while Eurasia dominates, this event is likely a basin-wide event that incorporates circum-Arctic changes in ice sheets. This event might coincide with Heinrich Event 6, a IRD event found in the North Atlantic and proposed to occur at ~60 ka [27].

Stage 3 is punctuated by two rapid events, E4 and E3 (Fig. 10). E4 occurs at 54 ka and has rates of 15 and 12 cm kyr^{-1} for 22JPC and 9JPC, respectively. In 9JPC, this period is associated with a strong peak in material sourced mainly to the ALIS and to a lesser extent IIS, with minimal input from SKIS (Fig. 10). 22JPC exhibits a strong increase in IIS sourced material, with lesser amounts of SKIS and ALIS. The difference in material received is likely due to proximity of the source regions to the core sites and the dominant transport pathways. The presence of this signal in both 9JPC and 22JPC indicates that this is a basin-wide event. The provenance coupled with an increase in >63 and >250 μm fractions indicates that this signal is a result of a large-scale calving event. A deglacial event has been documented to occur in early Stage 3 (Fig. 11) [20, 51]. The second Stage 3 event, Rapid event 3 (E3) is dated to ca. 39 ka and has rates of 25 and 10 cm kyr^{-1} for 22JPC and 9JPC, respectively (Fig. 10). There is an increase in coarse sediment texture through this period, indicating that sea ice and glacial ice transport is active (Fig. 11). 22JPC shows a small increase in ALIS sediment. The Fe grain data are not available for 9JPC at this interval. The timing of E3 coincides with Heinrich Event 4 that is independently dated to 38 [27] and 37 ka [7]; thus E3 might represent a central Arctic Heinrich-like event. A similar signal was identified from the Mendeleev Ridge in core 94BC16, with a timing of 38.9 ka and sourced to IIS (IRD7; [16]. The event identified in this study occurs just as the IIS source signal sharply decreases (Fig. 10).

Stage 2 is associated with two rapid accumulation events, the first is specific to 9JPC and the second (E2) is found in both 22JPC and 9JPC (Fig. 10). The 9JPC-specific pulse is assigned an age of approximately 27 kyr and has a sedimentation rate of >18 cm kyr^{-1} (Fig. 10). There is very little coarse material in this interval, but a large coarsening occurs just after this event (Fig. 11). Based on the Fe grain sources, only IIS and ALIS are contributing at this time (Fig. 11). Given the fine grain size in this interval, it is not surprising that smectite is high, while dolomite and plagioclase are both low, suggesting a Kara/Laptev Sea source (Fig. 12). A short 750 year event occurs at ca. 18 ka when sedimentation of >16 and >3 cm kyr^{-1} for 22JPC and 9JPC, respectively, marking the second Stage 2 rapid event (E2; Fig. 10). The signal is weak in 9JPC, but does potentially indicate the end of the LGM and the beginning of ice sheet disintegration. Both core locations experience increased amounts of material from IIS and SKIS, while 22JPC also receives material from ALIS (Fig. 10). Thus, it can be presumed that the glacial disintegration was contemporaneous from all regions. Also, given the provenance of the material we speculate that the ALIS material is bypassing 9JPC and the Stage 2 deglacial ice drift flows directly toward Fram Strait. The sediment grain size shows that near 18.5 ka the material was very fine (>99 % <63 μm) but is immediately followed by a sharp increase in coarse sediment (>20 % of >63 μm) (Fig. 11), suggesting a massive and short-lived calving event. At this same time, an intense freshwater event is identified in a sediment record from Yermak Plateau [59]. Additionally, this period corresponds to an IRD event identified in central Fram Strait cores that occurred between 19.3 and 17.4 ka [16]. These authors concluded that this IRD event contained Fe grains from the Laurentide and Innuitian simultaneously, which is also seen in this study.

The last rapid event identified, E1, occurred at 5.8 ka (Fig. 10). The overall sedimentation rates are not exceedingly high, but they do represent a short-lived increase over background rates. In 22JPC the rate increases to 5.5 cm kyr^{-1} and has identified sources from several circum-Arctic areas (Fig. 10). The rate for 9JPC increases to 3.6 cm kyr^{-1} with similar sources as 22JPC, except IIS is absent. There is a small, but significant increase in the sediment coarse fraction indicating that this is an increase in IRD deposition (Fig. 11). This period roughly coincides with the timing of Bond IRD Event 4, which is analogous to the 5.9 kyr event [8].

Conclusions/summary

The identification of these short-lived and rapid sediment accumulation events highlights the importance of this new central Arctic age model. The age model presented here is the first detailed age model for the central Arctic linked to the global δ^{18}O record that is able to resolve such rapid events. The results of this study raise questions regarding the timing and extent of various processes. For instance, the occurrence of freshwater events throughout the late Quaternary is more refined by this new age model, allowing for more constrained timings than previously published. Of course, stable isotope records would be needed to confirm these freshwater events. This refined timing is also true for major deglaciation events. The results here show that very high sedimentation rates can occur during glacial or stadial intervals, albeit for short intervals of time probably associated with iceberg discharges. The occasional extreme rates of sedimentation (>15 and as high as 20+ cm kyr^{-1}) have not been reported prior to this study for the Mendeleev Ridge area.

There are a number of improvements that can be made to this age model, most notably these are AMS-^{14}C dating of the Holocene and late Stage 2 and increased sampling resolution, though datable material is scarce. Additionally, an increased sampling resolution will reduce the impact of error and might allow for the identification of additional Heinrich Events and other IRD events similar to those events identified in MIS 3 and 4.

Acknowledgments The National Science Foundation funded this research. The XRF data were generated and provided by E. Council. We thank three anonymous reviewers for their helpful comments.

References

1. ACIA (2004) Impacts of a warming Arctic: Arctic climate impact assessment. Cambridge University Press, Cambridge
2. Adler RE, Polyak L, Ortiz JD, Kaufman DS, Channell JET, Xuan C, Grottoli AG, Sellen E, Crawford KA (2009) Sediment record from the western Arctic Ocean with an improved late Quaternary age resolution: HOTRAX core HLY0503-8JPC, Mendeleev Ridge. Glob Planet Change. doi:10.1016/j.gloplacha.2009.03.026
3. Alexanderson H, Backman J, Cronin TM, Funder S, Ingólfsson Ó, Jakobsson M, Landvik JY, Löwemark L, Mangerud J, März C, Möller P, O'Regan M, Spielhagen RF (2014) An Arctic perspective on dating Mid-Late Pleistocene environmental history. Quat Sci Rev 92:9–31
4. Backman J, Jakobsson M, Løvlie R, Polyak L, Febo LA (2004) Is the central Arctic Ocean a sediment starved basin? Quat Sci Rev 23:1435–1454
5. Backman J et al (2008) Age model and core-seismic integration for the Cenozoic Arctic Coring Expedition bsediments fromt he Lomonosov Ridge. Paleoceanography 23:PA1S03. doi:10.1029/2007PA001476
6. Bischof JA, Darby DA (1997) Mid to Late Pleistocene ice drift in the western Arctic Ocean: evidence for a different circulation in the past. Science 277:74–78
7. Bond GC, Lotti R (1995) Iceberg discharges into the North Atlantic on millennial time scales during the last glaciation. Science 267:1005–1010
8. Bond GC, Showers W, Cheseby M, Lotti R, Almasi P, deMenocal P, Priore P, Cullen H, Hajdas I, Bonani G (1997) A pervasive millennial-scale cycle in North Atlantic Holocene and glacial climates. Science 278:1257–1266

9. Clark DL, Whitman RR, Morgan KA, Mackey SD (1980) Stratigraphy and glacial-marine sediments of the Amerasian Basin, Central Arctic Ocean. Geol Soc Am Spec Pap 181:1–57
10. Council E (2012) Central Arctic lithostratigraphy: implication on sediment transport and paleoceanography. Dissertation, Wright State University
11. Cronin TM, Polyak L, Reed D, Kandiano ES, Marzen RE, Council EA (2013) A 600-ka Arctic sea-ice record from Mendeleev Ridge based on ostracodes. Quat Sci Rev. doi:10.1016/j.quascirev.2012.12.010
12. Darby DA (2003) Sources of sediment found in sea ice from the western Arctic Ocean, new insights into processes of entrainment and drift patterns. J Geophys Res 108:3275
13. Darby DA, Bischof JF (1996) A statistical approach to source determination of lithic and Fe-oxide grains: an example from the Alpha Ridge, Arctic Ocean. J Sediment Res 66:599–607
14. Darby DA, Bischof J (2004) A Holocene record of changing Arctic Ocean ice drift, analogous to the effects of the Arctic Oscillation. Paleoceanography 19:PA1027. doi:10.1029/2003PA000961
15. Darby DA, Zimmerman P (2008) Ice-rafted detritus events in the Arctic during the last glacial interval and the timing of the Innuitian and Laurentide ice sheet calving events. Polar Res 27:114–127
16. Darby DA, Naidu AS, Mowatt TC, Jones GA (1989) Sediment composition and sedimentary processes in the Arctic Ocean. In: Herman Y (ed) The Arctic seas: climatology, oceanography, geology, and biology. VanNostrand Reinhold, New York, pp 657–720
17. Darby DA, Bischof J, Cutter G, de Vernal A, Hillaire-Marcel C, Dwyer G, McManus J, Osterman L, Polyak L, Poore R (2001) New record of pronounced changes in Arctic Ocean circulation and climate. EOS Trans 49:603–607
18. Darby DA, Bischof JF, Spielhagen RF, Marshall SA, Herman SW (2002) Arctic ice export events and their potential impact on global climate during the late Pleistocene. Paleoceanography. doi:10.1029/2001PA000639
19. Darby DA, Polyak L, Jakobsson M, Berger G, Lövlie R, Perovich D, Grenfell T, Kikuchi T, Tateyama K (2006a) HLY0503 cruise report. http://sci.odu.edu/oceanography/research/hotrax/leg2/HYL0503_cruise_rpt.pdf
20. Darby DA, Polyak L, Bauch H (2006b) Past glacial and interglacial conditions in the Arctic Ocean and marginal seas, a review. In: Wassman P (ed) Structure and function of contemporary food webs on Arctic shelves: a Pan-Arctic comparison. Progr Oceanogr 71:129–144
21. Darby DA, Ortiz J, Polyak L, Lund S, Jakobsson M, Woodgate RA (2009) The role of currents and sea ice in both slowly deposited central Arctic and rapidly deposited Chukchi-Alaskan margin sediments. Glob Planet Change 68:58–72
22. Darby DA, Myers WB, Jakobsson M, Rigor I (2011) Modern dirty sea ice characteristics and sources: the role of anchor ice. J Geophys Res. doi:10.1029/2010JC006675
23. Darby DA, Ortiz JD, Grosch CE, Lund SP (2012) 1,500-year cycle in the Arctic Oscillation identified in Holocene Arctic sea-ice drift. Nature Geo. doi:10.1038/NGEO1629
24. Darby DA, Myers W, Herman S, Nicholson B (2015) Chemical fingerprinting, a precise and efficient method to determine sediment sources. J Sediment Res 85:247–253. doi:10.2110/jsr.2015.17
25. Eberl DD (2003) User guide to RockJock—a program for determining quantitative mineralogy from X-ray diffraction data. Revised 2009. U.S. Geological Survey Open-File Report, OF 03-78, 56 pp (RockJock version 10)
26. Eberl DD (2004) Quantitative mineralogy of the Yukon River system: changes with reach and season, and determining sediment provenance. Am Miner 89:1784–1794
27. Hemming SR (2004) Heinrich events: massive late Pleistocene detritus layers of the North Atlantic and their global climate imprint. Rev Geophys. doi:10.1029/2003RG000128
28. IPCC (2013) Climate change 2013: the physical science basis. In: Stocker TF, Qin D, Plattner G-K, Tignor M, Allen SK, Boschung J, Nauels A, Xia Y, Bex V, Midgley PM (eds) Contribution of working group I to the fifth assessment report of the intergovernmental panel on climate change. Cambridge University Press, Cambridge, UK and New York, NY, USA, 1535 pp. doi:10.1017/CBO9781107415324
29. Jakobsson M, Løvlie R, Al-Hanbali H, Arnold E, Backman J, Mörth M (2000) Manganese and color cycles in Arctic Ocean sediments constrain Pleistocene chronology. Geology 28:23–26
30. Jakobsson M, Løvlie R, Arnold EM, Backman J, Polyak L, Knutsen J-O, Musatov E (2001) Pleistocene stratigraphy and paleoenvironmental variation from Lomonosov Ridge sediments, central Arctic Ocean. Glob Planet Change 31:1–22
31. Jakobsson M, Polyak L, Edwards M, Kleman J, Coakley B (2008) Glacial geomorphology of the Central Arctic Ocean: the Chukchi Borderland and the Lomonosov Ridge. Earth Surf Process Landf 33:526–545
32. Jakobsson M et al (2012) The international bathymetric chart of the Arctic Ocean (IBCAO) version 3.0. Geophys Res Lett. doi:10.1029/2012GL052219
33. Jakobsson M et al (2013) Arctic Ocean glacial history. Quat Sci Rev 92:40–67
34. Kaufman D, Polyak L, Adler R, Channell J, Xuan C (2008) Dating late Quaternary planktonic foraminifer Neogloboquadrina pachyderma from the Arctic Ocean by using amino acid racemization. Paleoceanography 23:PA3224
35. Kleman J, Jansson K, De Angelis H, Stroeven AP, Hättestrand C, Alm G, Glasser N (2010) North American ice sheet build-up during the last glacial cycle, 115–21 kyr. Quat Sci Rev 29:2036–2051
36. Knies J, Vogt C (2003) Freshwater pulses in the eastern Arctic Ocean during Saalian and Early Weichselian ice-sheet collapse. Quat Res 60:243–251
37. Knies J, Vogt C, Stein R (1999) Late Quaternary growth and decay of the Svalbard/Barents Sea ice sheet and paleoceanographic evolution in the adjacent Arctic Ocean. Geo-Mar Lett 18:195–202
38. Knies J, Kleiber HP, Matthiessen J, Müller C, Nowaczyk N (2001) Marine ice-rafted debris records constrain maximum extent of Saalian and Weichselian ice-sheets along the northern Eurasian margin. Global Planet Change 31:45–64
39. Knies J, Matthiessen J, Mackensen A, Stein R, Vogt C, Frederichs T, Nam S-I (2007) Effects of Arctic freshwater forcing on thermohaline circulation during the Pleistocene. Geology 35:1075–1078
40. Lang N, Wolff EW (2011) Interglacial and glacial variability from the last 800 ka in marine, ice and terrestrial archives. Clim Past 7:361–380
41. Levitan MA, Stein R (2008) History of sedimentation rates in the glacial zone of sedimentation during the last 130 ka. Lith Min Res 1:74–86 **(in Russian)**
42. Lisiecki LE, Raymo ME (2005) A Pliocene–Pleistocene stack of 57 globally distributed benthic δ^{18}O records. Paleoceanography 20:PA1003. doi:10.1029/2004PA001071
43. Löwemark L, Jakobsson M, Mörth M, Backman J (2008) Arctic Ocean Mn contents and sediment color cycles. Polar Res 27:105–113
44. Löwemark L, O'Regan M, Hanebuth T, Jakobsson M (2012) Late Quaternary spatial and temporal variability in Arctic deep-sea bioturbation and its relation to Mn-cycles. Paleogeogr Paleoclimatol Paleoecol 365:192–208
45. Löwemark L, März C, O'Regan M, Gyllencruetz R (2014) Arctic Ocean Mn-stratigraphy: genesis, synthesis and inter-basin

correlation. Quat Sci Rev 92:97–111. doi:10.1016/j.quascirev.2013.11.018

46. Macdonald R, Gobeil C (2012) Manganese sources and sinks in the Arctic Ocean with reference to periodic enrichments in basin sediments. Aquat Geochem 18:565–591
47. McManus J, Berelson WM, Klinkhammer GP, Johnson KS, Coale KH, Anderson RF, Kumar N, Burdige DJ, Hammond DE, Brumsack HJ, McCorkle DC, Rushdi A (1998) Geochemistry of barium in marine sediments: implications for its use as a paleoproxy. Geochim Cosmochim Acta 62:3453–3473
48. Moore DM, Reynolds RC (1997) X-ray diffraction and the identification and analysis of clay minerals. Oxford University Press, New York
49. Not C, Hillaire-Marcel C (2010) Time constraints from 230Th and 231 Pa data in late Quaternary, low sedimentation rate sequences from the Arctic Ocean: an example from the northern Mendeleev Ridge. Quat Sci Rev 29:3665–3675
50. Nowaczyk NR, Antonow M, Knies J, Spielhagen RF (2003) Further rock magnetic and chronostratigraphic results on reversal excursions during the last 50 ka as derived from northern high latitudes and discrepancies in precise AMS ^{14}C dating. Geophys J Int 155:1065–1080
51. Polyak L, Curry WB, Darby DA, Bischof J, Cronin TM (2004) Contrasting glacial/interglacial regimes in the western Arctic Ocean as exemplified by a sedimentary record form the Mendeleev Ridge. Palaeogeogr Palaeoclimatol Palaeoecol 203:73–93
52. Polyak L, Darby DA, Bischof J, Jakobsson M (2007) Stratigraphic constraints on late Pleistocene glacial erosion and deglaciation of the Chukchi Margin, Arctic Ocean. Quat Sci Res 67:234–245
53. Polyak L et al (2009) Late Quaternary stratigraphy and sedimentation patterns in the western Arctic Ocean. Glob Planet Change 68:5–17. doi:10.1016/j.gloplacha.2009.03.014
54. Poore RZ, Ishman S, Phillips RL, McNeil DH (1994) Quaternary stratigraphy and paleoceanography of the Canada Basin, western Arctic Ocean. U.S. Geol Surv Bull, vol 2080, 32 pp
55. Schlitzer R (2012) Ocean data view. http://odv.awi.de
56. Sellen E, Jakobsson M, Frank M, Kubik PW (2009) Pleistocene variations of beryllium isotopes in central Arctic Ocean sediment cores. Glob Planet Change 68:38–47
57. Sellén E, O'Regan M, Jakobsson M (2010) Spatial and temporal Arctic Ocean depositional regimes: a key to the evolution of ice drift and current patterns. Quat Sci Rev 29:3644–3664
58. Spielhagen RF, Erlenkeuser H (1994) Stable oxygen and carbon isotope ratios in planktic foraminifers from the Arctic Ocean surface sediments: reflection of the low salinity surface water layer. Mar Geol 119:227–250
59. Spielhagen RF, Baumann K-H, Erlenkeuser H, Nowaczyk NR, Nørgaard-Pedersen N, Vogt C, Weiel D (2004) Arctic Ocean deep-sea record of northern Eurasian ice sheet history. Quat Sci Rev 23:1455–1483
60. Srondon J, Drits VA, McCarty DK, Hsieh JCC, Eberl DD (2001) Quantitative mineral analysis by powder X-ray diffraction from random preparations. Clays Clay Miner 49:514–528
61. Stärz M, Gong X, Stein R, Darby DA, Kauker F, Lohmann G (2012) Glacial shortcut of Arctic sea-ice transport. Earth Planet Sci Lett 357:257–267
62. Stein R, Matthiessen J, Niessen F, Krylov R, Nam S, Bazhenova E (2010) Towards a better (litho-) stratigraphy and reconstruction of Quaternary paleoenvironment in the Amerasian Basin (Arctic Ocean). Polarfors 79:97–121
63. Stoner JS, Jennings A, Kristjánsdóttir GB, Dunhill G, Andrews JT, Hardardóttir J (2007) A paleomagnetic approach toward refining Holocene radiocarbon-based chronologies: paleoceanographic records from the north Iceland (MD99-2269) and east Greenland (MD99-2322) margins. Paleoceanography 22:PA1209. doi:10.1029/2006PA001285
64. St. Onge G, Stoner JS (2011) Paleomagnetism near the North Magnetic Pole: a unique vantage point for understanding the dynamics of the geomagnetic field and its secular variations. Oceanography 24:42–50. doi:10.5670/oceanog.2011.53
65. Svendsen JI, Alexanderson H, Astakhov VI et al (2004) Late Quaternary ice sheet history of Northern Eurasia. Quat Sci Rev 23:1229–1271
66. Vogt C (1997) Regional and temporal variations of mineral assemblages in Arctic Ocean sediments as climatic indicator during glacial/interglacial changes. Rep Pol Res 251:1–309
67. Vogt C, Knies J, Spielhagen RF, Stein R (2001) Detailed mineralogical evidence for two nearly identical glacial/deglacial cycles and Atlantic water advection to the Arctic Ocean during the last 90,000 years. Glob Planet Change 31:23–44
68. Wahsner M, Müller C, Stein R, Ivanov G, Levitan M, Shelekhova E, Tarasov G (1999) Clay-mineral distribution in surface sediments of the Eurasian Arctic Ocean and continental margin as indicator for source areas and transport pathways—a synthesis. Boreas 28:215–233
69. Xuan C, Channell JET (2010) Origin of apparent magnetic excursions in deep-sea sediments from Mendeleev–Alpha Ridge, Arctic Ocean. Geochem Geophys Geosyst 11:2. doi:10.1029/2009GC002879
70. Xuan C, Channell JET, Polyak L, Darby DA (2012) Paleomagnetism of Quaternary sediments from Lomonosov Ridge and Yermak Plateau: implications for age models in the Arctic Ocean. Quat Sci Rev 32:48–63